



**HAL**  
open science

## Testing the role of environmental effects on the initial mass function of low-mass stars

Belinda Damian, Jessy Jose, Manash R. Samal, Estelle Moraux, Swagat R. Das, Sudeshna Patra

► **To cite this version:**

Belinda Damian, Jessy Jose, Manash R. Samal, Estelle Moraux, Swagat R. Das, et al.. Testing the role of environmental effects on the initial mass function of low-mass stars. *Monthly Notices of the Royal Astronomical Society*, 2021, 504, pp.2557-2576. 10.1093/mnras/stab194 . insu-03705302

**HAL Id: insu-03705302**

**<https://insu.hal.science/insu-03705302>**

Submitted on 6 Aug 2022

**HAL** is a multi-disciplinary open access archive for the deposit and dissemination of scientific research documents, whether they are published or not. The documents may come from teaching and research institutions in France or abroad, or from public or private research centers.

L'archive ouverte pluridisciplinaire **HAL**, est destinée au dépôt et à la diffusion de documents scientifiques de niveau recherche, publiés ou non, émanant des établissements d'enseignement et de recherche français ou étrangers, des laboratoires publics ou privés.

# Testing the role of environmental effects on the initial mass function of low-mass stars

Belinda Damian <sup>1</sup>★, Jessy Jose <sup>1</sup>★, Manash R. Samal <sup>2</sup>, Estelle Moraux,<sup>3</sup> Swagat R. Das <sup>1</sup> and Sudeshna Patra<sup>1</sup>

<sup>1</sup>Indian Institute of Science Education and Research (IISER) Tirupati, Rami Reddy Nagar, Karakambadi Road, Mangalam (P.O.), Tirupati 517 507, India

<sup>2</sup>Physical Research Laboratory (PRL), Navrangpura, Ahmedabad 380 009, Gujarat, India

<sup>3</sup>Univ. Grenoble Alpes, CNRS, IPAG, F-38000 Grenoble, France

Accepted 2021 January 20. Received 2021 January 20; in original form 2020 May 28

## ABSTRACT

In the star-formation process, the vital impact of environmental factors such as feedback from massive stars and stellar density on the form of the initial mass function (IMF) at the low-mass end is yet to be understood. Hence a systematic highly sensitive observational analysis of a sample of regions under diverse environmental conditions is essential. We analyse the IMF of eight young clusters (<5 Myr), namely IC 1848-West, IC 1848-East, NGC 1893, NGC 2244, NGC 2362, NGC 6611, Stock 8, and Cygnus OB2, which are located at the Galactocentric distance ( $R_g$ ) range  $\sim 6$ –12 kpc along with the nearby cluster IC 348 using deep near-IR photometry and *Gaia* DR2. These clusters are embedded in massive stellar environments of radiation strength  $\log(L_{\text{FUV}}/L_{\odot}) \sim 2.6$ –6.8,  $\log(L_{\text{EUV}}) \sim 42.2$ –50.85 photon  $\text{s}^{-1}$ , with stellar density in the range of  $\sim 170$ –1220 star  $\text{pc}^{-2}$ . After structural analysis and field decontamination we obtain an unbiased uniformly sensitive sample of pre-main-sequence members of the clusters down to the brown-dwarf regime. The lognormal fit to the IMF of nine clusters gives the mean characteristic mass ( $m_c$ ) and  $\sigma$  of  $0.32 \pm 0.02 M_{\odot}$  and  $0.47 \pm 0.02$ , respectively. We compare the IMF with that of low- and high-mass clusters across the Milky Way. We also check for any systematic variation with respect to the radiation field strength and the stellar density as well with  $R_g$ . We conclude that there is no strong evidence for an environmental effect in the underlying form of the IMF of these clusters.

**Key words:** stars: formation – stars: low-mass – stars: luminosity function, mass function – stars: pre-main-sequence.

## 1 INTRODUCTION

Molecular clouds provide the sites for stellar cluster formation. Their fragmentation results in the birth of stars over a broad spectrum ranging from high-mass stars of several tens of solar masses to low-mass sub-stellar objects with masses below  $0.07 M_{\odot}$ . The mass of a star at birth is an important physical quantity as it determines the subsequent evolutionary path of the star and is a vital parameter in framing the star-formation theories. The distribution of the stellar mass at birth, known as the stellar initial mass function (IMF), is a fundamental property of star formation. In addition to enhancing our knowledge of the formation and evolution of stars, the shape of the IMF imposes a constraint on the star-formation process (e.g. Krumholz 2014; Offner et al. 2014) and it is a key quantity in many astrophysical studies. Therefore, a thorough understanding of its accurate shape is imperative (see various reviews by Bastian, Covey & Meyer 2010; Jeffries 2012; Kroupa et al. 2013; Offner et al. 2014; Moraux 2016).

The pioneering work of Salpeter (1955), which formulated the power-law distribution for the high-mass end of the IMF, led to the onset of a great deal of observational and theoretical studies, carried out to understand the form of the IMF across different star-

forming environments. In recent years, the advancement of large telescopes has aided in extending these studies to the least massive stars and sub-stellar objects. The increasing focus in this field is substantiated by the various functional forms of the IMF available in the literature. For the Milky Way, Salpeter (1955) originally proposed a single power-law form for the high-mass side ( $\geq 1 M_{\odot}$ ) of the IMF, which is generally approximated as  $\frac{dN}{dM} \propto m^{-\alpha}$ , with  $\alpha = 2.35$ . More updated forms of the IMF mainly include the multicomponent power-law functions (Kroupa 2001), the tapered power-law form (De Marchi, Paresce & Portegies Zwart 2005, 2010), and the lognormal distribution (Chabrier 2003). Although the above functional forms agree well with each other at the high-mass end ( $> 1 M_{\odot}$ ), they deviate towards the low-mass end (see Offner et al. 2014) and, as a result, we lack a model of star formation that predicts the IMF of a stellar population produced by a given molecular cloud.

Most of the observational studies on the IMF focus on the high-mass end, which appears to have a fairly uniform distribution across the Milky Way disc and the local solar neighbourhood (Bastian et al. 2010; Offner et al. 2014; Moraux 2016 for a review). However, there have been claims of a non-universal IMF in the Milky Way as well as in external galaxies. Dib (2014), through comparative analysis of the mass function of eight galactic clusters using Bayesian statistics, states that the IMF is not universal. Similarly, a non-universal IMF is observed in extreme environments such as in the Galactic Centre

\* E-mail: belin\_93@yahoo.in (BD); jessyvjose1@gmail.com (JJ)

(e.g. Lu et al. 2013; Hosek et al. 2019), in the most massive elliptical galaxies (e.g. van Dokkum & Conroy 2010; Cappellari et al. 2012), and in the least luminous Milky Way satellites (e.g. Geha et al. 2013; Gennaro et al. 2018). Guszejnov, Hopkins & Graus (2019) showed that the current IMF models in the literature either fail to reproduce the observed variations in the IMF of dwarf and elliptical galaxies or violate the universality of the IMF in the Milky Way. On the other hand, theoretical studies suggest that changes in the IMF depend on local environmental conditions such as protostellar outflows, magnetic field, turbulence, or radiation feedback (see Krumholz et al. 2016 and references therein). However, all these claims of a non-standard IMF are still highly debated, demanding a more homogeneous approach to derivation of the IMF for a sample of targets in diverse conditions. This uncertainty in the nature of the IMF and its potential dependence on the environment poses one of the most challenging problems in modern astrophysics. Observations of the IMF of a variety of environments are essential to test the relative influence of various environmental factors such as gas temperature, stellar feedback, and turbulence on the IMF (e.g. Hosek et al. 2019).

In recent years, studies to explore the low-mass and sub-stellar end of the IMF have advanced remarkably, particularly in the nearby star-forming regions (e.g. Taurus, IC 348, 25 Ori; see Luhman, Esplin & Loutrel 2016; Luhman 2018; Suárez et al. 2019). Unfortunately, these nearby ( $< 500$  pc) environments are poor analogues of the diverse star-forming conditions, where metallicity varies or massive stellar feedback dominates. Moreover, most of the nearby star-forming regions contain mainly low-mass stars with no or very few massive stars, with the exception of the ONC, which is the only massive star-forming region within 500 pc. On the other hand, most of the regions with embedded massive stars are located further away and their IMF determination extends usually down to a few solar masses only, and in a few selected cases reaches masses close to the hydrogen-burning limit. For example, the studies on Westerlund 1 by Andersen et al. (2017) and on Trumpler 14 by Rochau et al. (2011) extended down to  $\sim 0.15 M_{\odot}$  and Mužić et al. (2017) estimated the IMF in RCW 38 down to  $0.02 M_{\odot}$ , while the IMF has been characterized down to  $0.4 M_{\odot}$  in NGC 3603 (Stolte et al. 2006; Harayama, Eisenhauer & Martins 2008). However, still lacking is a systematic uniform analysis of the low-mass stellar IMF of a statistically rich sample of Galactic young clusters of diverse properties and located at various environmental conditions.

The study of the low-mass IMF is extremely challenging due to the lack of a complete and clean sample of young members, which is an absolute essential for its accurate estimation. Also, studies on individual regions are often biased by different sources of uncertainties such as the use of different evolutionary models, reddening laws, membership criteria, and non-uniform sensitivity of observations rather than the variation between individual clusters (Mužić et al. 2019). With the understanding that stars in young clusters have roughly the same age and metallicity and are located at the same distance, the assumption that their observed present-day mass functions (PDMFs) are a fair representation of their IMFs seems reasonable. In particular, rich or moderately rich young cluster samples are of particular importance for IMF studies since such clusters play host to a thousand to a few thousand stars, and are better for robust statistical measurements. Moreover, such young clusters of a few Myr are not expected to be dynamically evolved. The effect of mass segregation due to dynamical evolution is more pronounced in old clusters and can preferentially remove low-mass members from the cluster centre. Young clusters are largely free of the effects of dynamical evolution although primordial mass segregation is expected to some extent.

In order to explore the role of environmental factors in the form of the low-mass stellar IMF, in this study we have selected a sample of young clusters of diverse properties in terms of their stellar density, number of associated massive stars, and location at various Galactocentric distances. The environmental conditions in these regions are significantly different from those in nearby star-forming regions. The main focus of this study is to explore the low-mass part of the IMF (i.e.  $< 3 M_{\odot}$  and down to the brown-dwarf regime) by obtaining an unbiased uniformly sensitive sample of members in these regions and to correlate it with the well studied mass distributions in nearby star-forming regions and young massive clusters. The selected clusters are young enough for dynamical processes and stellar evolution not to have significantly altered the stellar-mass distribution, and the physical conditions of the birth environment have not been completely erased. In this work, we do not perform corrections for binary stars, as they might not affect the overall shape of the IMF significantly. The studies in young clusters by Harayama et al. (2008), Zeidler et al. (2017), Mužić et al. (2017), Suárez et al. (2019) show that the effect of binarity in IMF calculations is not very pronounced as the single-star IMF and the system IMF agree within errors.

The paper is structured as follows. In Section 2, we describe the various properties of the sample clusters in our study and the NIR photometry data sets used for the analysis. Section 3 explains the estimation of cluster fundamental parameters such as centre, radius, distance, reddening, and age, field-star decontamination process, and membership criteria leading to the estimation of the IMF. Section 4 discusses the IMFs estimated for the regions under study and their comparison with other well studied regions. Section 5 summarizes the various results obtained.

## 2 SAMPLE SELECTION AND DATA

### 2.1 Sample selection

To make a comprehensive statistical analysis of the form of the IMF in diverse environmental conditions, we have selected eight young clusters from various studies (Chauhan et al. 2011; King et al. 2013; Jose et al. 2017; Kuhn et al. 2019). We select the clusters satisfying the following criteria: i) age  $< 5$  Myr with massive O and B type stars at its centre, ii) a rich population of pre-main-sequence (PMS) stars with relatively low interstellar reddening, iii) availability of deep *JHK* data from 4 m class telescopes, iv) spatial distribution over a wide range of Galactocentric distances. The clusters included in this work are IC 1848-East, IC 1848-West, NGC 1893, NGC 2244, NGC 2362, NGC 6611, Stock 8, and the bright cluster at the centre of the Cygnus OB2 association (which we refer as Cygnus OB2 hereafter). The details are given in Table 1. Below we discuss the individual clusters, the massive stars associated with them, and their basic characteristics such as age, distance, reddening etc. Fig. 1 shows the spatial distribution of the clusters in this study with respect to the Sun and the Galactic Centre, where  $R_0$ , the Galactocentric distance of the Sun, is taken to be 8.34 kpc (Reid et al. 2014). *JHK* colour composite images of the clusters are given in online Appendix A.

#### 2.1.1 IC 1848-West and IC 1848-East

Westerhout 5 or W5 is one of the three major star-forming clouds in the W3/W4/W5 giant molecular cloud (GMC) of the Cassiopeia OB6 association (see Jose et al. 2016). W5 has two prominent H II regions associated with the clusters IC 1848-West and IC 1848-East. Both

**Table 1.** Details of the sample clusters.

Sample	Data set	Cluster		Control field		Data completeness					
		RA (deg)	Dec. (deg)	RA (deg)	Dec. (deg)	<i>J</i> band (mag)	<i>H</i> band (mag)	<i>K</i> band (mag)	<i>J</i> band ( $M_{\odot}$ )	<i>H</i> band ( $M_{\odot}$ )	<i>K</i> band ( $M_{\odot}$ )
IC 1848-West	NEWFIRM (Mayall Telescope)	42.7958	+60.4019	44.9642	+60.7584	19.0	18.5	18.5	0.04	0.04	0.03
IC 1848-East	NEWFIRM (Mayall Telescope)	44.8458	+60.5667	44.9642	+60.7584	18.5	17.5	17.0	0.08	0.11	0.11
NGC 1893	WFCAM (UKIRT, MYSIX)	80.7064	+33.4273	80.6741	+33.5531	18.5	17.5	17.5	0.19	0.22	0.17
NGC 2244	WFCAM (UKIRT, GPS)	97.9808	+04.9431	97.9842	+05.1100	17.5	17.0	16.5	0.07	0.07	0.07
NGC 2362	WFCAM (UKIRT, MYSIX)	109.6865	-24.9582	109.3938	-24.6989	19.0	18.5	18.5	0.02	0.02	0.02
NGC 6611	WFCAM (UKIRT, MYSIX)	274.6700	-13.7900	274.4976	-13.7934	19.0	18.0	17.0	0.04	0.05	0.07
Stock 8	WFCAM (UKIRT, GPS)	82.0373	+34.4244	82.2884	+34.5069	18.5	18.0	17.5	0.09	0.08	0.09
Cygnus OB2	WFCAM (UKIRT, GPS)	308.2827	+41.2155	308.5783	+41.4213	18.5	17.5	17.0	0.12	0.10	0.09

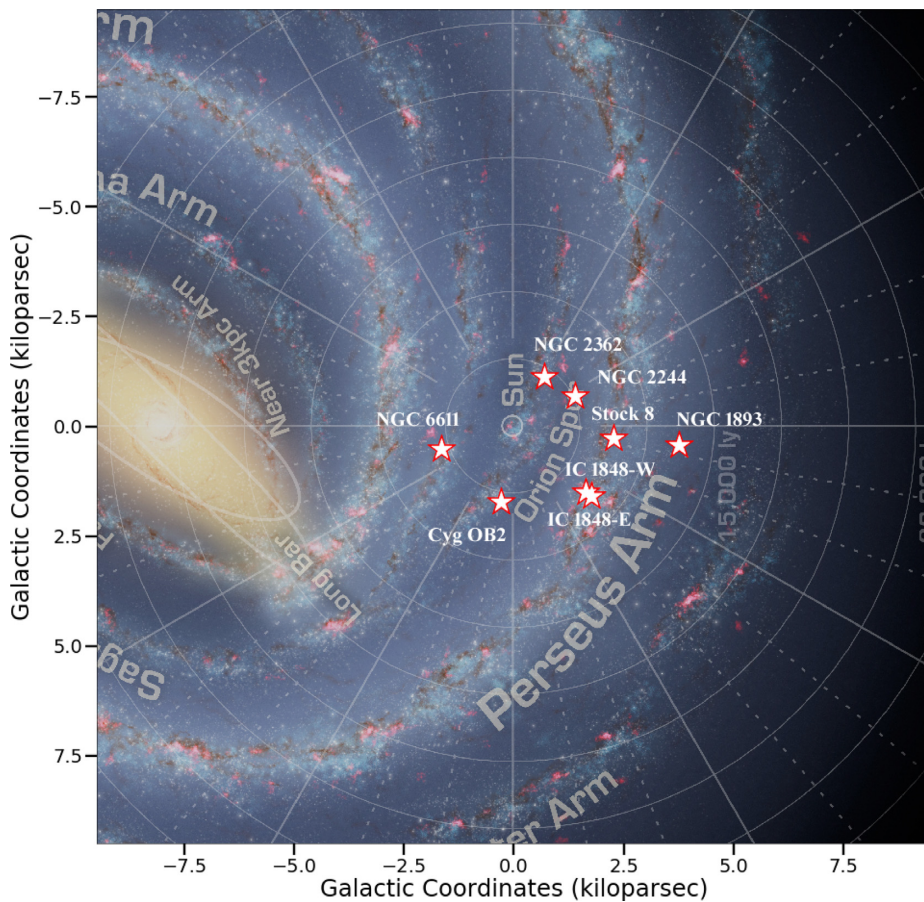


**Figure 1.** Spatial distribution of the clusters in the study with respect to the Sun and the Galactic Centre.  $R_0$  (distance of the Sun from the Galactic Centre) is taken to be 8.34 kpc (Reid et al. 2014). The image is adapted from <sup>1</sup>, credit by Robert Hurt, IPAC; Bill Saxton, NRAO/AUI/NSF.

clusters have massive stars at their centre ionizing the environment around them by strong UV radiation (Koenig et al. 2008). Hence

these clusters serve as ideal targets to study the star-formation process within the feedback environment of massive stars.

The cluster IC 1848-West has two O stellar groups dominating at its centre (HD 17505 and HD 17520) and each one is a multiple system. The multiple system HD 17505 contains at least four O stars (O6.5 III((f)), O7.5 V((f)), O7.5 V((f)), O8.5 V) that are apparently

<sup>1</sup><https://www.universetoday.com/102616/our-place-in-the-galactic-neighborhood-just-got-an-upgrade>

gravitationally bound (Hillwig et al. 2006; Raucq et al. 2018 and references therein). The binary system HD 17520 is associated with O8 V and O9:Ve stars (Sota et al. 2011). The cluster IC 1848-West is located at a distance of  $2.2 \pm 0.2$  kpc (Moffat 1972; Lim et al. 2014a) with mean interstellar reddening  $A_V = 2.05 \pm 0.17$  mag (Lim et al. 2014a). Using PMS evolutionary models for low-mass stars, an average age of  $\sim 3$  Myr has been estimated in this cluster (Lim et al. 2014a).

IC 1848-East is primarily ionized by HD 18326, a binary system of spectral types O6.5 V((f))z and O9/B0 V (Sota et al. 2014) located at the centre of the cluster. The  $A_V$  value in the cluster is in the range of  $\sim 1.9$ – $2.5$  mag with a mean age for young stellar objects of  $\sim 1$ – $2$  Myr and is located at a distance of  $\sim 2.1 \pm 0.3$  kpc (Chauhan et al. 2011).

### 2.1.2 NGC 1893

NGC 1893 is a young open cluster embedded in the IC 410 H II region at the centre of the Auriga OB2 association located towards the Galactic anti-centre. There are five O-type stars (HD 242926 – O7 V; HD 242908 – O4 V((f)); LS V +34°15 – O5.5 V((f)); BD +33°1025A – O7 V; HD 242935 – O7.5 V((f))) embedded in the cluster (Negueruela et al. 2007). Previous studies estimate the cluster to be at a distance of  $\sim 3$ – $6$  kpc (Tapia et al. 1991; Marco, Bernabeu & Negueruela 2001; Sharma et al. 2007; Prisinzano et al. 2011; Pandey et al. 2013). The mean  $A_V$  value of the cluster is in the range of  $\sim 1.5$ – $1.9$  mag (Sharma et al. 2007; Prisinzano et al. 2011; Lim et al. 2014b) and is  $\sim 1.4$ – $1.9$  Myr old (Prisinzano et al. 2011; Lim et al. 2014b). Though located at a far distance, the population of massive stars and relatively low interstellar reddening make this region an ideal target to study the effect of external factors on star formation (Negueruela et al. 2007).

### 2.1.3 NGC 2244

NGC 2244 is a young cluster associated with the star-forming region Monoceros OB2 (Mon OB2) association. This system is located in the north-west quadrant of the Rosette Molecular Cloud complex, which is one of the most massive GMCs in the Milky Way (Chen, de Grijs & Zhao 2007). The cluster houses seven massive O-type stars (HD 46223 – O4 V((f)); HD 46150 – O5 V((f))z; HD 46485 – O7 Vn; HD 46056 – O8 Vn; HD 46149-1 – O8 V; HD 46149-2 – O8.5–9 V; HD 46202 – O9.5 V) along with numerous B-type stars that ionize the neighbourhood (Martins et al. 2012). The estimated distance to the cluster is in the range of  $\sim 1.3$ – $1.7$  kpc (Perez, The & Westerlund 1987; Hensberge, Pavlovski & Verschueren 2000; Park & Sung 2002; Mužić et al. 2019). The  $A_V$  value is  $\sim 1.4$ – $1.7$  mag (Massey, Johnson & Degioia-Eastwood 1995; Li 2005; Bonatto & Bica 2009) and the average age is  $\sim 2$ – $3$  Myr (Pérez 1991; Hensberge et al. 2000; Bonatto & Bica 2009) for the cluster.

### 2.1.4 NGC 2362

NGC 2362 is a young star cluster located in the third Galactic quadrant, dominated by the fourth magnitude O9 Ib multiple star  $\tau$  Cma and nearly three dozen B-type stars distributed in a volume of  $\sim 3$  pc radius (Dahm & Hillenbrand 2007). Using optical photometry, Moitinho et al. (2001) obtained the distance to the cluster as  $\sim 1.5$  kpc and an age of  $\sim 3$ – $6$  Myr. They also show that the cluster has a well defined locus of PMS stars in the colour–magnitude diagram that

makes it an ideal laboratory for stellar evolution studies. Considering the young age of the cluster, the region has a rather low uniform  $A_V$  value of  $\sim 0.31$  mag (Moitinho et al. 2001; Dahm 2005; Delgado et al. 2006).

### 2.1.5 NGC 6611

The young cluster NGC 6611 is part of the Ser OB I association in the Sagittarius spiral arm and is responsible for ionizing the well known nebula M16 (the Eagle Nebula) in the W37 molecular cloud (Hillenbrand et al. 1993). This is the only cluster directed towards the Galactic Centre in our list. Structurally the region has several nebular features, the so-called elephant trunks (Pillars of Creation), at the tips of which newborn stars are visible (Bonatto, Santos & Bica 2006). There are 13 O-type stars embedded in the cluster (Hillenbrand et al. 1993; Evans et al. 2005). The distance to the cluster is estimated to be in the range of  $\sim 1$ – $2$  kpc (Hillenbrand et al. 1993; Bonatto et al. 2006; Dufton et al. 2006; Guarcello et al. 2007). Various studies have shown that the cluster is  $\sim 1$ – $4$  Myr old (Hillenbrand et al. 1993; Bonatto et al. 2006; Dufton et al. 2006) and the extinction in the region varies in the range of  $\sim 1.4$ – $3.1$  mag (Oliveira, Jeffries & van Loon 2009) with an average value of  $\sim 2.6$  mag (Guarcello et al. 2007).

### 2.1.6 Stock 8

Stock 8 is located within the H II region of IC 417 (Sh2-234) in the Auriga constellation of the Perseus arm. It is surrounded by 12 massive OB-type stars and is probably part of a large OB association (Jose et al. 2008; Marco & Negueruela 2016; Jose et al. 2017). Various distance estimations of the cluster lie in the range of  $\sim 2.05$ – $2.8$  kpc (Jose et al. 2008; Marco & Negueruela 2016). The reddening within the cluster region ( $A_V$ ) has been estimated to be in the range of  $\sim 1.2$ – $1.9$  mag and age between 1 and 5 Myr (Jose et al. 2008). Using PMS evolutionary model fitting, Jose et al. (2017) obtain a median age of  $\sim 3.0$  Myr with an age spread of  $\sim 2$  Myr for the cluster. The star LS V +34°23 with spectral type O8 II(f) is likely to be the main source of ionization for the H II region (Marco & Negueruela 2016).

### 2.1.7 Young cluster within Cygnus OB2

Cygnus OB2 (Cyg OB2) is a young massive OB association in the Cygnus X region (Winter, Clarke & Rosotti 2019). It contains many massive stars up to  $\sim 100 M_\odot$  (Wright, Drew & Mohr-Smith 2015) that contribute to the strong FUV radiation fields in the region. Based on infrared studies, Knödlseeder (2000) estimated the total number of O-type stars within Cygnus OB2 as  $120 \pm 20$ , claiming this to be the largest population of O stars found in a Galactic massive stellar association. The  $A_V$  values of member stars range from  $\sim 5$ – $20$  mag (Knödlseeder 2000). Based on the most massive dwarf stars in the bulk of the cluster, Hanson (2003) estimates an average age of  $\sim 2$  Myr with a spread of 1 Myr. However, Wright et al. (2015) suggest that the majority of star formation in Cyg OB2 occurred more or less continuously between 1 and 7 Myr ago. Using the *Gaia* parallax and fitting a two-component Gaussian model, Berlanas et al. (2019) obtained the median distance to the cluster as 1755 pc. Bica, Bonatto & Dutra (2003) identify two young clusters towards the centre of the rich compact association Cygnus OB2, named Object 1 and 2, and in this study we analyse the southern cluster, Object 1.

## 2.2 Deep NIR photometry

We have gathered deep NIR photometry in the  $J$ ,  $H$ , and  $K$  bands from various sky surveys and observations taken using the 4 m class telescopes. Our main goal is to obtain uniformly sensitive deep photometry data sets for all the regions in order to sample the stellar masses down to  $\sim 0.08 M_{\odot}$ . Fields of view of all the regions in the  $JHK$  bands are given in online Appendix A. Below we describe the various data sets used for individual clusters; these are also listed in Table 1.

For the clusters NGC 2244, Stock 8, and Cygnus OB2, we took the photometry from UKIDSS (United Kingdom Infrared Deep Sky Survey; Lawrence et al. 2007) DR6 GPS (Galactic Plane Survey) observed using the WFCAM (Wide Field Camera) on the 3.8 m UKIRT (United Kingdom Infrared Telescope). We limit the catalogue to sources with goodness of fit ( $p_{\text{star}} > 0.9$ , which gives the probability of the source being a star, and  $\text{PriOrSec}(m) = 1$ , which removes the duplicated sources located in the overlapping regions between different arrays in a WFCAM tile (Lucas et al. 2008).

For the clusters NGC 1893, NGC 2362, and NGC 6611, we use the photometry from the MYStIX survey (Massive Young Star-Forming Complex Study in Infrared and X-ray; Feigelson et al. 2013) observed using the WFCAM on the UKIRT. We restrict our catalogue to sources with  $J$ ,  $H$ , and  $K$  magnitudes flagged as ‘O’. This constraint removes the bad pixels and non-stellar sources (King et al. 2013). Apart from the individual source selection criterion for the various catalogues, to ensure photometric accuracy, we use only those sources with photometric uncertainty within 0.2 mag in the  $J$ ,  $H$ , and  $K$  bands.

For the clusters in the W5 complex (IC 1848-East and IC 1848-West), we obtain the data from the NOAO archive.<sup>2</sup> The observations in the  $J$ ,  $H$ , and  $K$  bands were conducted using the wide-field IR imager NEWFIRM (NOAO Extremely Wide Field Infrared Imager; Probst et al. 2004) with the 4 m Mayall Telescope at Kitt Peak National Observatory, Arizona (PI: Guy Stringfellow). The NEWFIRM camera includes four InSb  $2048 \times 2048$  pixel arrays arranged in a  $2 \times 2$  pattern and the field of view is  $28 \times 28$  arcmin with a pixel scale of 0.4 arcsec. Using the NEWFIRM Science Pipeline (Swaters, Valdes & Dickinson 2009), the standard processing tasks of dark correction, flat-fielding, sky subtraction, and bad-pixel masking were performed and we obtained the final calibrated, stacked, and mosaicked images in three bands from the archive. The FWHM values of the images were in the range of 0.8–1.0 arcsec. Using the DAOFIND task in IRAF we obtained the list of point sources in the  $K$  band with signal  $5\sigma$  above the background. The  $5\sigma$  detection criterion was useful to avoid any false detection or artefacts in the image. The list of sources was again visually checked to exclude any spurious detection. The same source list was used for the  $J$  and  $H$  bands as well. We performed point spread function photometry of these sources using the ALLSTAR routine of IRAF (e.g. Jose et al. 2016, 2017). For absolute photometric calibration, we used the Two Micron All Sky Survey (2MASS) catalogue (Cutri et al. 2003) of those sources with quality flag ‘A’ in all three bands. The match radius used to obtain the common sources in the 2MASS and NEWFIRM catalogues was 1.0 arcsec. The zero-point correction term with respect to 2MASS photometry has been applied to our NEWFIRM photometry for individual bands in order to calibrate it. The calibration accuracy was within 0.05–0.07 mag for all three bands. Our final NEWFIRM photometry list includes only those sources with  $S/N > 5$  and photometry uncertainty  $< 0.2$  mag in all three bands.

For the above clusters, we have examined a  $\sim 20 \times 20$  arcmin area and a nearby control field (see Section 3.3 for details) to study the cluster properties. In general, our photometry has a wide dynamic range of  $\sim 12$ – $20$  mag in the  $J$  band. The saturation limits of individual data sets differ depending on various factors such as sky background, seeing, exposure time etc. across different observations. Considering the saturation limit of UKIDSS photometry, we exclude sources brighter than 13 mag in the  $J$  band (Lucas et al. 2008) for our analysis. Since this study focuses only on the low-mass end of the IMF ( $< 3 M_{\odot}$ ), this cut-off will not affect our results.

## 3 ANALYSIS AND RESULTS

Section 2.1 shows that numerous studies were carried out in the past to examine the various physical parameters such as radius, distance, reddening, and age of each cluster. Most of these analyses show a large range in the parameters estimated. However, a uniform method to analyse these properties is essential in order to exclude any bias in the estimation of IMF. In this section we use the deep  $JHK$  photometry to analyse the various physical properties of the clusters.

### 3.1 Data completeness

Photometric data often suffer from data incompleteness, mostly towards the fainter end. There are various factors contributing to this, such as sensitivity of different observations, crowding, and variable extinction. In order to evaluate the completeness of the photometry used in this analysis, we plot histograms of the sources detected within the area considered for the analysis for each cluster. The turnover point in the histogram distribution is generally considered as the pointer for  $\sim 90$  per cent completeness (e.g. Willis et al. 2013; Samal et al. 2015; Maia, Moraux & Joncour 2016; Jose et al. 2017). In the cases where the bin trailing the turnover point is more than 90 per cent of the peak value, then that magnitude is taken as the completeness limit (Jose et al. 2016). The  $\sim 90$  per cent completeness limits thus estimated for all the clusters in this study are given in Table 1. Fig. 2 shows the sample completeness histograms in the  $J$  (left) and  $K$  bands (right) of two different clusters, one for each of the telescopes used in this study (i.e. the UKIRT and Mayall telescopes) (see Section 2.2). The completeness histograms corresponding to the control fields of these clusters are represented in Fig. B1 (see Appendix B). From Figs 2 and B1 it is clear that the completeness of the cluster and control fields is comparable. Our estimates for the completeness of the data in all three bands agree with the 90 per cent completeness limits mentioned in the UKIDSS GPS catalogue details (Lucas et al. 2008).

The above method of stellar counting for data completeness measurements should be appropriate for most of the area in the cluster. However, the local stellar surface density and/or the presence of bright stars within the cluster region can have an effect on the completeness of the data (e.g. Maia et al. 2016; Andersen et al. 2017). A more rigorous analysis of data incompleteness by the artificial star simulations by Maia et al. (2016) and Jose et al. (2017) shows that the data incompleteness from the stellar count method and artificial star simulations is correlated for most of the area of interest. However, photometry can be incomplete towards the cluster centre in extremely crowded regions (e.g. Maia et al. 2016). In order to analyse any spatial variation, we measured the completeness by the artificial star method within annular radii of 1 arcmin from the centre of Stock 8 outwards. The completeness varies from  $\sim 85$ – $95$  per cent from the inner to outer radius of the cluster with an

<sup>2</sup><http://archive1.dm.noao.edu/search/query/>

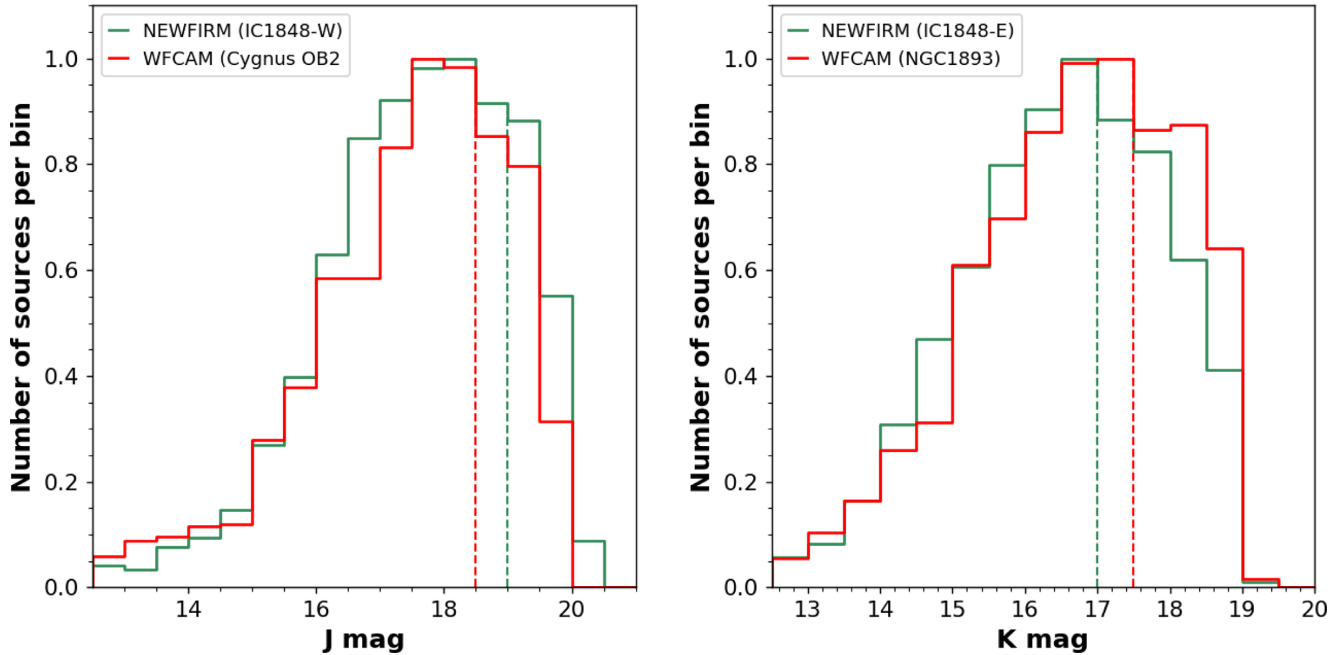


**Figure 2.** Normalized sample histograms showing the completeness limits of the data used from different telescopes in the *J* band (left) and *K* band (right). The turnover point in the distribution serves as a proxy for the completeness limit of the data. The dashed lines mark the  $\sim 90$  per cent completeness limit of the photometry.

average of  $\sim 90$  per cent for the magnitude bin 17–18 in the *K* band, which is in agreement with our histogram method (see Table 1). In this paper we do not account for spatial variation of incompleteness across the cluster regions. We use the photometry down to the 90 per cent completeness limits given in Table 1 for follow-up analysis. The corresponding mass completeness limits, estimated using the evolutionary models of Baraffe et al. (2015) after incorporating the distance, reddening, and age of the respective clusters, are also given in Table 1 (see Sections 3.4, 3.5, and 3.6 for details). In general, our photometry is complete down to  $\sim 0.08 M_{\odot}$  for most of the regions except NGC 1893.

### 3.2 Cluster centre and radius

One of the critical steps in membership analysis and IMF construction is determining the radial extent of the cluster. To delineate the cluster area we determine the stellar surface density and consider the central region with a density higher than that of the surroundings (which includes both the foreground and background field stars) as the cluster limit. There are two basic approaches for density estimation, parametric and non-parametric techniques. If the cluster probability density function is known then parametric methods are useful. Since this is unlikely, we rely on non-parametric methods (Nambiar et al. 2019). We employ two non-parametric approaches to determine the cluster radius: the star-count method and the *k*-nearest-neighbours method.

#### 3.2.1 Star-count method

One commonly used method to determine the cluster radius is to analyse the variations in the stellar surface density (e.g. Baba et al. 2004; Ojha et al. 2011). In this regard, the star-count method is a simple yet robust approach. In this method, we grid the sample region into bins of equal size and estimate the individual bin density, i.e. the number of sources in each bin divided by the bin area. For

uniformity, we consider a bin size of 0.3 pc for all the clusters under study (i.e. the angular sizes of the bins varied from 15–45 arcsec depending on the distance to the cluster). Choosing the appropriate bin size is critical since a small bin prohibits meaningful statistics and a large bin hides the underlying cluster features. After various trials using different bin sizes, 0.3 pc seemed to be ideal for both the nearby and distant clusters. Fig. 3 shows a Hess diagram of the spatial density distribution of a sample cluster, IC 1848-West. The density in each bin is smoothed over with nearby bins by interpolation and the colour gradient indicates the density variation across the cluster area. In order to obtain the background density, we consider a control field for each cluster that is at the same Galactic latitude as the cluster. The coordinates of the control field for each cluster are given in Table 1. We measure the mean ( $\mu$ ) and standard deviation ( $\sigma_{\text{bg}}$ ) values of the stellar density distribution within the control field. The cluster is assumed to lie within a region defined by  $\mu + 3\sigma_{\text{bg}}$ . We restrict the radius to  $3\sigma$  in order to reduce the field contaminants as well as to avoid the differential reddening in a larger area. The radius of the circle covering this area and the highest-density bin within it are taken as the cluster radius and centre, respectively. The cluster radii obtained through this method are tabulated in Table 2.

#### 3.2.2 Nearest-neighbours method

Unlike the star-count method, which depends on the density gradient between the cluster and the background field, the *k*-nearest-neighbours method is a more reliable and well acclaimed method to estimate the stellar surface density. The method, introduced by Casertano & Hut (1985), gives the generalized form of the *j*th nearest-neighbour surface density for a star as:

$$\rho_j = \frac{j-1}{\pi r_j^2} \quad (1)$$

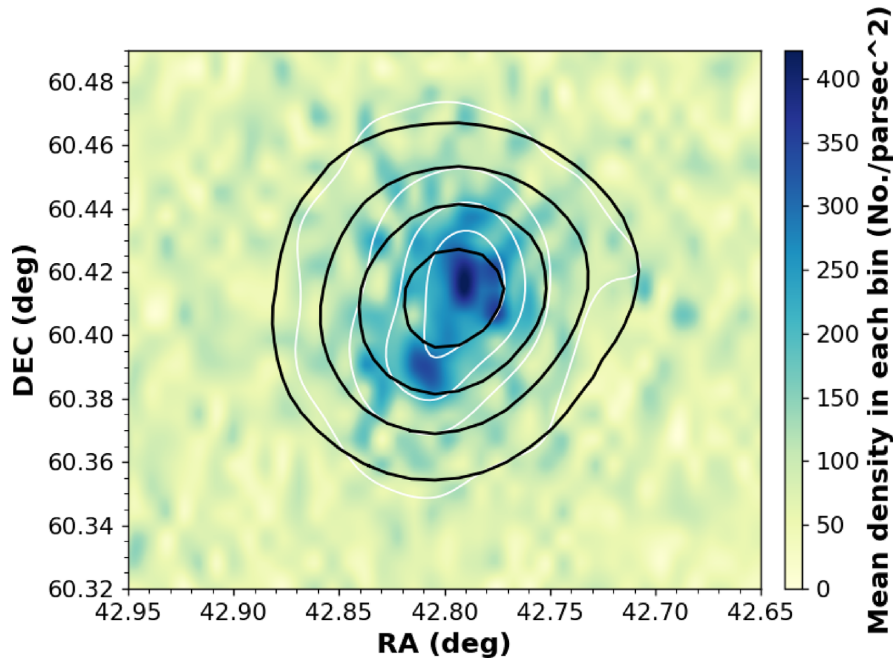


**Figure 3.** Surface density plot of sample cluster IC 1848-West. Black contours and white contours mark the  $3\sigma$ ,  $5\sigma$ ,  $7\sigma$ , and  $9\sigma$  levels above the background density estimated by the nearest-neighbours method and star-count method respectively.

**Table 2.** Physical parameters of the clusters.

Cluster	Star count	Radius		Mean	Mean	Distance (d)	Distance ( $R_g$ )	$A_k$	Median age
		Nearest neighbours	(arcmin)						
IC 1848-West	4.2	3.8	4.0	2.6	$2220 \pm 420^b$	$10\,080 \pm 350$	$0.14 \pm 0.05$	$2 \pm 1$	
IC 1848-East	2.9	3.1	3.0	2.0	$2380 \pm 510^b$	$10\,230 \pm 430$	$0.21 \pm 0.07$	$2 \pm 1$	
NGC 1893			$3.0^a$	3.3	$3790 \pm 600^c$	$12\,110 \pm 600$	$0.15 \pm 0.07$	$2 \pm 3$	
NGC 2244	4.6	4.4	4.5	2.0	$1550 \pm 95^c$	$9750 \pm 90$	$0.10 \pm 0.06$	$2 \pm 3$	
NGC 2362	3.6	3.4	3.5	1.4	$1332 \pm 70^c$	$9110 \pm 40$	$0.04 \pm 0.03$	$3 \pm 2$	
NGC 6611	4.6	4.0	4.3	2.2	$1740 \pm 125^c$	$6690 \pm 120$	$0.29 \pm 0.11$	$2 \pm 1$	
Stock 8	2.5	2.9	2.7	1.8	$2290 \pm 460^b$	$10\,620 \pm 460$	$0.15 \pm 0.07$	$3 \pm 2$	
Cygnus OB2	2.8	3.2	3.0	1.5	$1755 \pm 320^d$	$8220 \pm 10$	$0.54 \pm 0.08$	$2 \pm 2$	

Notes. <sup>a</sup>Sharma et al. (2007).

<sup>b</sup>This work.

<sup>c</sup>Kuhn et al. (2019); the means of their error values are shown.

<sup>d</sup>Berlanas et al. (2019); the mean error value is used.

where  $r_j$  is the distance from any given star to its  $j$ th neighbour. Similar to the star-count method where choosing the appropriate bin size is critical, in this method, using the right  $j$  value is essential. If the  $j$  value is too small then insignificant subclustering or false groupings become prominent. At the same time, if  $j$  is large then small-scale high-density subgroups will be overlooked. Hence for detecting substructures within a cluster a lower  $j$  value is preferable, while higher  $j$  values may be used to trace large-scale structures (Schmeja 2011). For our analysis, we varied the values of  $j$  as 10, 15, and 20;  $j = 15$  was found to be optimal to trace the radius of the clusters. Similar to the star-count method, we estimate the background counts ( $\mu$  and  $\sigma$ ) by averaging the density of the control field. In Fig. 3 we overplot contours for the  $3\sigma$ ,  $5\sigma$ ,  $7\sigma$ , and  $9\sigma$  levels above the background density estimated by this method. The radius of the  $3\sigma$  contour is considered the cluster radius and the location of highest density the cluster centre. The cluster radii obtained through this method are tabulated in Table 2.

The radius estimated using the star-count method is consistent with that estimated using the nearest-neighbours method for all the clusters except NGC 1893. NGC 1893 is an elongated star-forming region with two prominent cometary globules towards its north-east, making the outer edge of the cluster significantly reddened (Sharma et al. 2007). In order to avoid these features we adopt a cluster radius of 3 arcmin from Sharma et al. (2007). The means of the cluster centre and radius measured from the star-count and nearest-neighbours methods have been adopted as the cluster centre and radius for each cluster. The adopted central coordinates and the radius of each cluster are listed in Tables 1 and 2, respectively. For further analysis, we use the data within the radius of each cluster. In young clusters the majority of their stars lie within a few core radii (see Sharma et al. 2007; Jose et al. 2008); thus the effect of halo stars lying beyond the radius adopted here on the IMF estimation is unlikely to be significant. We discuss this point in Section 3.8.

### 3.3 Field-star decontamination

Field stars in astronomical studies are those that do not belong to the celestial system being observed. They can be the foreground or background sources that appear in the same field of view as the object. An initial step in our IMF analysis is to identify the probable cluster members by removing the field-star contaminants from the data sets. This membership determination is crucial for estimating the IMF because both PMS and dwarf foreground stars overlap in the colour–magnitude diagrams (CMDs; e.g. Jose et al. 2017). There are various methods for assessing the membership probabilities of the sources in a cluster utilizing the positions, proper motions, radial velocities, spectroscopy, or multiband photometry of the stars (e.g. Panwar et al. 2017; Dutta et al. 2018; Bhardwaj et al. 2019; Herczeg et al. 2019; Jose et al. 2020 and references therein). It is commonly accepted that precise membership probabilities are obtained by using kinematic parameters of the sources. However, our clusters lie beyond the solar neighbourhood and astrometric data in general tend to have high uncertainties towards the fainter end and hence constrain our options of low-mass membership analysis. Without kinematic or spectroscopic data for the clusters, a main method to separate the members from the field stars is by statistical subtraction using a nearby control field (e.g. Jose et al. 2017; Kaur et al. 2020). For all the clusters in this study, we choose a control field of similar area in the cluster vicinity (see Table 1). The control field for each cluster was selected based on the assumption that it is not located far away from the cluster, so that its Galactic field stellar distribution would be similar to that in the cluster. However, it cannot be too close to the cluster centre, which may include some of the cluster members. We avoided regions with too much nebulosity, which is a signature of active star formation. We also excluded the regions with young stellar objects associated with these clusters that are listed in the previous studies (Section 2.1). The control fields thus selected are  $\sim 7$ – $22$  arcmin away from the cluster centre (see Table 1). As the clusters IC 1848-East and IC 1848-West lie in the same star-forming complex, we consider the same control field for both of them, taken from the corner of the NEWFIRM image of IC 1848-East. Since the control fields are relatively close to the cluster regions, the reddening variation between the two regions is negligible and hence we assume that a similar amount of field contaminants exist in the cluster region as well as in the control field. In order to validate this assumption of similar extinction distribution both for the cluster and control fields, in panel 3 of the figures given in online Appendix C we have overplotted the CMDs of the cluster and control field regions. It is evident from all the figures that the control field sequence exactly overlays the field sequence of the cluster region and there is no significant offset between the two distributions. This shows that the extinction differences between the cluster and control fields are negligible and hence we could perform statistical subtraction without giving any additional correction in the extinction values of the control field.

The field stars were statistically removed by the following steps. We use the  $(J - H)$  versus  $J$  CMD for both the cluster as well as the control field regions within the radius determined from Section 3.2. We prefer this combination because the  $J$  and  $H$  bands are least affected by NIR excess emission from the circumstellar disc around young stellar objects. We then divide the colour and magnitude axes into bins of size 0.1 and 0.2 mag, respectively. For every source in each bin of the control field, the corresponding source in the cluster region is considered as a background star and is removed. By repeating this process for all the bins in the field CMD, we obtain the background-subtracted sources in the target cluster. In Fig. 4, we show the  $(J - H)$  versus  $J$  CMDs of a sample cluster IC 1848-West

and its control field. The CMDs of all other clusters are given in online Appendix C. A comparison of cluster and field region CMDs in Fig. 4 shows that the sequence of stars seen on the left-hand side in both figures is the field stellar population and the additional sequence towards the right in the cluster CMD is the locus of the candidate PMS members of the cluster (see Jose et al. 2017). The PMS branch is well defined and lies separate from the field-star distribution between  $\sim 14$  and  $18$  mag in the  $J$  band and merges with the field sequence at fainter magnitudes, as the low-mass PMS sources have an intrinsic blueish colour as evident in the PMS models (Baraffe et al. 2015). All the clusters in our list have similar well defined PMS branches (see online Appendix C). Also, the PMS branch has a relatively narrow distribution of points, revealing that the differential extinction within the clusters is minimal (see Section 3.5 for details), unlike other very young clusters that are still embedded in molecular clouds (e.g. Jose et al. 2016; Mužić et al. 2017; Panwar et al. 2017; Bik et al. 2019). The width of the dispersion of points in colour may be due to variability, binarity, age spreads, or photometric uncertainties (see Jose et al. 2017; Kuhn et al. 2017 for details). In the right-hand panel of Fig. 4, the field-decontaminated (i.e. statistically subtracted) CMD of the cluster IC 1848-West is shown (see online Appendix C for the rest of the regions).

In Fig. 5, Hess diagrams (which show the relative density distribution of stars in the CMD) of the cluster IC 1848-West (left), control field (middle), and the field-star decontaminated cluster region (right) are shown. The Hess diagrams clearly show a density enhancement along the PMS branch that remains the same after field decontamination.

The right-hand panel in Fig. 4 shows the distinct presence of the PMS population along with a few scattered sources. These scattered sources are most likely field contaminants that were not removed due to the statistical uncertainty in our decontamination process. In order to refine the decontamination process and clean our final catalogue, we define the locus of the PMS branch by fitting a Gaussian function along the colour axis and for bins of 0.5 mag in the  $J$  band. Since the PMS branch is roughly vertical, we fit the Gaussian perpendicular to the distribution, i.e. along the colour axis. Also, since the sequence is vertical, it is not affected by any variation in colour due to binarity of sources and hence it is safe to assume a Gaussian distribution of sources. We then use the peak of the Gaussian curve as the mean locus of the PMS branch and restrict the membership to sources that lie within  $3\sigma$  of the mean. The dashed curve in Fig. 4 marks the mean locus of the PMS population and the continuous curves show the  $3\sigma$  limits. At the brighter end, we limit the PMS selection at the saturation limit. At the fainter end, we limit the source inclusion boundary at 90 per cent completeness, where the PMS branch mostly merges with the field sequence. This limitation does not bias our results as we are only interested in the low-mass population ( $3$ – $0.08 M_{\odot}$ ) of the clusters.

Galactic interstellar extinction maps (Marshall et al. 2006) suggest that beyond the cluster NGC 6611, at a distance between  $\sim 2.8$  and  $3.5$  kpc, there is an extinction jump from  $A_k \sim 0.6$  to  $1.4$  mag, which is consistent with the location of the Scutum–Crux spiral arm towards the Galactic Centre (Vallée 2008). Using evolutionary tracks in the  $J - H$  versus  $J$  CMD, Oliveira et al. (2009) show that the dense population on the right of the PMS branch with redder colours ( $J - H \sim 1.5$ – $3$  mag) is mainly background sources located in this spiral arm falling in the line of sight of NGC 6611. This hypothesis is also explained in Guarcello et al. (2007) who showed that, due to dust associated with the Eagle nebula in which the cluster is embedded, the background field stars are more reddened than the cluster stars. The

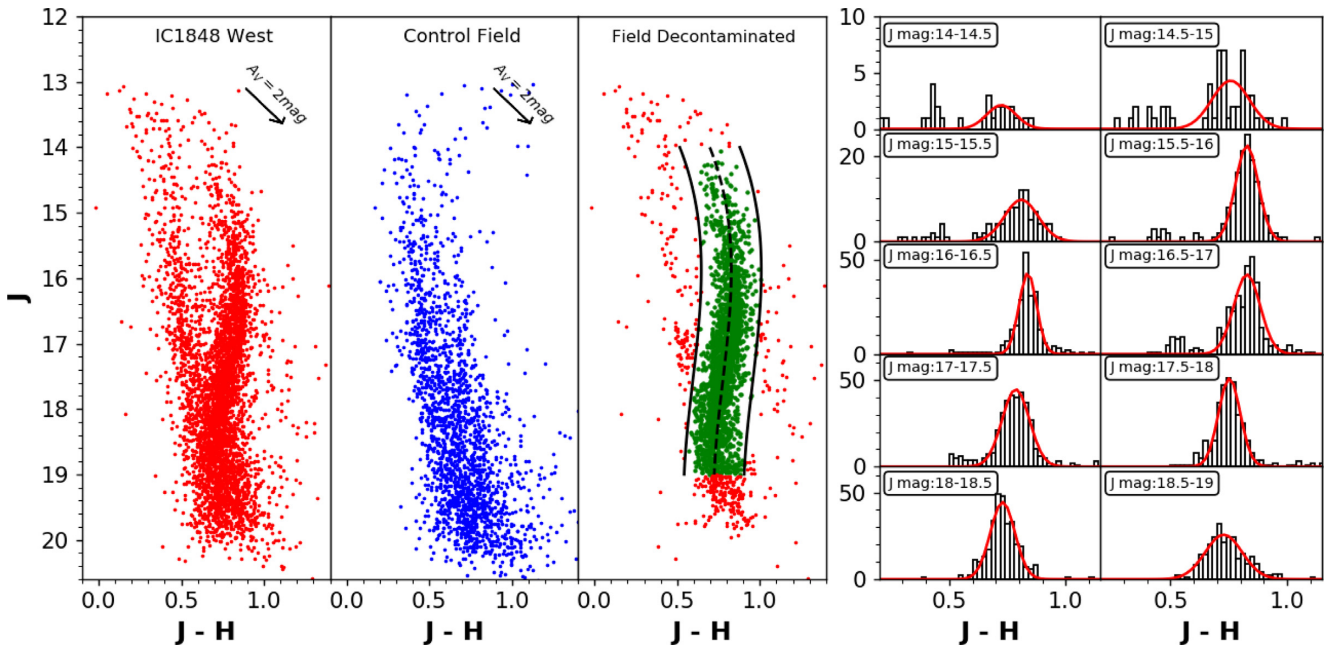


**Figure 4.** Left:  $J - H$  versus  $J$  CMD of the sample cluster IC 1848-West for all the sources within the radius (left), nearby control field (middle), and CMD after field decontamination (right). The reddening vector for  $A_V = 2$  mag is also shown. Right: Histograms showing the distribution along the  $J - H$  axis for every 0.5 mag strip of the  $J$  band. The mean of the Gaussian fit (red curve) gives the mean locus of the PMS population in that magnitude bin. The dashed curve in the field-decontaminated CMD (left) represents the interpolation of the PMS locus of each bin and the continuous curves mark the  $3\sigma$  deviation from the mean locus. The candidate PMS members within the  $3\sigma$  distribution are highlighted in green.

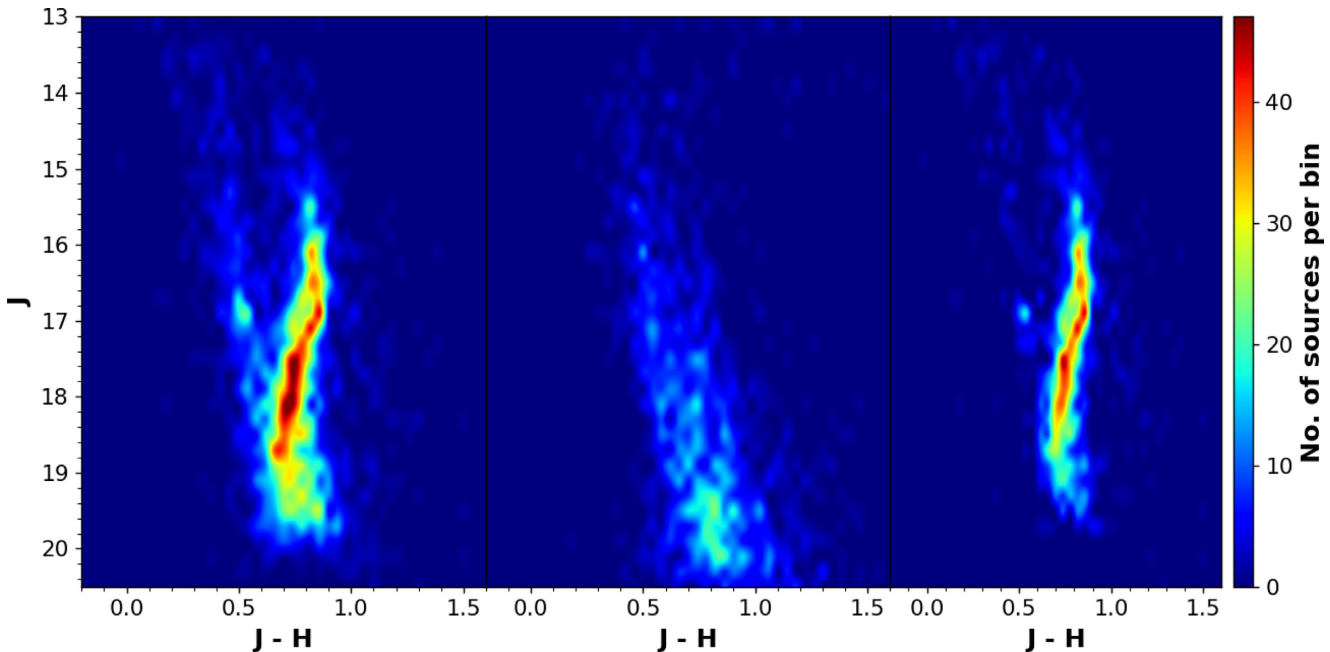


**Figure 5.** Hess diagrams of  $J - H$  versus  $J$  CMD of sample cluster IC 1848-West (left), control field (middle) and cluster region after field-star decontamination (right). The colour bar indicates the number of sources in each bin of size 0.04 along  $(J - H)$  and 0.2 along  $J$ .

$J - H$  versus  $J$  CMD (see online Appendix C) of NGC 6611 shows this dense reddened background population. Due to the presence of this dense background population, the Gaussian peak of the PMS branch shifts towards the reddened sources at  $J - H \sim 2.0$  mag and below  $J = 16$  mag. In order to obtain an unbiased locus of the PMS

sources, we make a subset of the field-decontaminated catalogue by excluding these background sources by giving a colour cut-off of 1.5 mag in  $(J - H)$ . We refit the Gaussian with the refined catalogue and follow the procedure mentioned above for field decontamination of NGC 6611.

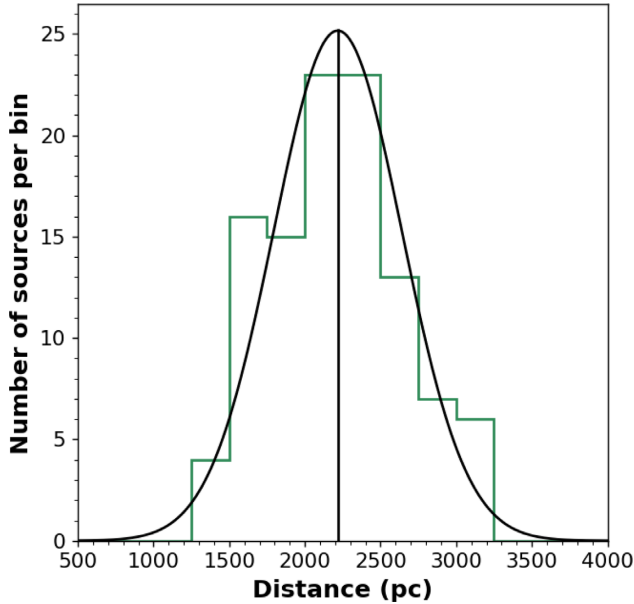


**Figure 6.** Histogram distribution of distance of the candidate members in the sample cluster IC 1848-West; the curve represents the Gaussian fit. The mean of this Gaussian fit is considered as the distance to the cluster.

### 3.4 Distance estimation

There have been various distances estimated for each cluster in the past (see Section 2.1). In order to constrain the distance to each cluster uniformly, we use the data from *Gaia* Data Release 2 (Gaia Collaboration et al. 2016, 2018). *Gaia* data provide precise five-parameter astrometry (position, parallax, and proper motion) for more than 1.3 billion sources in the Milky Way. Many studies have been carried out using the *Gaia* parallaxes to estimate the distance to the star-forming regions (e.g. Berlanas et al. 2019; Herczeg et al. 2019). Kuhn et al. (2019) estimate the system parallax using the weighted median of individual stellar parallax measurements of *Gaia* and obtained the distances for the NGC 1893, NGC 2362, NGC 2244, and NGC 6611 clusters. We adopt the distances estimated by Kuhn et al. (2019) for these clusters (see Table 2). Using the *Gaia* parallax and parametrized model inference approach, Berlanas et al. (2019) identify two different stellar groups superposed in the Cygnus OB2 association. They observe the main Cygnus OB2 group at  $\sim 1760$  pc and a foreground group at  $\sim 1350$  pc. We adopt a distance of 1760 pc for the Cygnus OB2 cluster for our analysis.

For other clusters (i.e. IC 1848-West, IC 1848-East, and Stock 8) distance estimates using *Gaia* data are unavailable and we estimate the distances as follows. Using the *Gaia* parallax and a probabilistic approach, Bailer-Jones et al. (2018) derive the distances to all the *Gaia* sources taking care of the non-linearity in parallax transformation. We obtain their distance catalogue for sources with parallax uncertainty  $\leq 0.2$  within each cluster radius (see Section 3.2). We cross-match this distance catalogue with the field-decontaminated candidate PMS members (Section 3.3) using a match radius of 1.2 arcsec (Kuhn et al. 2019). We model a Gaussian curve over the distance distribution of these sources. We converge the data to sources within  $1\sigma$  deviation from the peak (i.e. 68 per cent confidence interval of the mean) and the mean and standard deviation of the refitted Gaussian distribution are considered as a proxy for the distance and its uncertainty, respectively. Fig. 6 shows a histogram of the distance to the candidate PMS sources in the sample cluster IC 1848-West

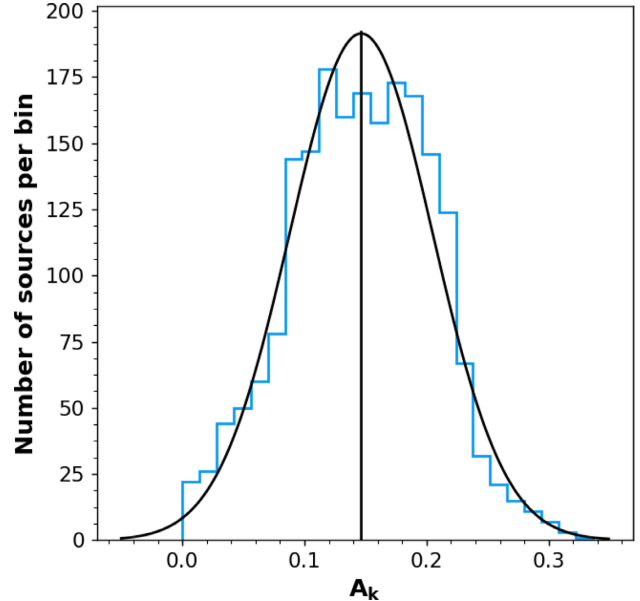


**Figure 7.** Histogram showing the extinction distribution of the candidate members in the sample cluster IC 1848-West. The mean of the Gaussian fit is taken as the mean extinction value for the cluster.

for the converged data set along with Gaussian fitting. We cross-check our distance calculation by following the method described in Kuhn et al. (2019) for the above-listed common clusters. The values derived from both methods agree within 100 pc, which confirms the accuracy of our distance estimation. The distances thus used for individual regions are listed in Table 2. Using the relation from Xue et al. (2008) we have calculated the Galactocentric distance ( $R_g$ ) of the clusters and they are given in Table 2.

### 3.5 Extinction estimation

There are two main factors that contribute to the extinction of stars in a cluster. One is the interstellar medium in the foreground of the cluster along the line of sight and the other is the localized parental molecular cloud in which the cluster is embedded. The extinction measurements of individual clusters by various studies are mentioned in Section 2.1. In order to measure the extinction to the clusters uniformly, we follow the below method. We use the field-decontaminated candidate PMS members (Section 3.3) for the extinction estimation of each cluster. We derive the *K*-band extinction towards the cluster using the extinction ratio  $\frac{A_k}{A_v} = 0.114$  adopted from Cardelli, Clayton & Mathis (1989), (i.e.  $A_k = E(J - H) \times 0.807$ , where  $E(J - H) = (J - H)_{\text{obs}} - (J - H)_{\text{int}}$ ). The mean value of the  $(J - H)$  colours of K- and M-type stars from Pecaut & Mamajek (2013) is taken as the intrinsic colour (i.e.  $(J - H)_{\text{int}} = 0.6$  mag). Since the spread in the intrinsic colours of low-mass objects are of the order of photometric uncertainty, this is a fair approximation. Fig. 7 shows the histogram distribution of  $A_k$  of all the candidate PMS sources for the sample cluster IC 1848-West. The mean and standard deviation of the Gaussian fit are taken as the extinction and uncertainty values, respectively for all the clusters. We compare the above estimated mean extinction with that of the extinction measured by dereddening to the intrinsic  $(H - K)_0$  colour (i.e. 0.2 mag) for the cluster IC 1848-W and within uncertainty limit, both the values agree very well. The mean and errors of the extinction estimated for each cluster are listed in Table 2. Except Cygnus OB2, all the clusters have

$A_K$  in the range of  $\sim 0.05$ – $0.3$  mag (i.e.  $A_V < 2.5$  mag) with a narrow spread of  $\sim 0.07$  mag, showing that the reddening variation within the adopted radius is relatively low in the clusters. The estimated extinction values of the clusters are used for dereddening the sources to measure their age and mass.

### 3.6 Age

The age and age spread of young clusters are fundamental parameters that are among the most uncertain and difficult to constrain, especially at young ages (see Soderblom et al. 2014 for a review). Knowledge of these two time-scales is critical for understanding the evolutionary appearance and state of a cluster and its star-formation history (Lada & Lada 2003). Although we acknowledge that stars take different lengths of time to reach the zero-age main sequence depending on their mass, in the simplest approximation, we picture all stars within a single cluster as having coalesced out of the interstellar medium at the same time. However, several studies have shown non-coeval stellar evolution of the young star-forming regions with a spread in the age estimates (e.g. Jose et al. 2016; Kraus et al. 2017; Panwar et al. 2018 etc.). The classic method for estimating the age is through use of the Hertzsprung–Russell diagram (HRD), where the positions of member stars are compared with the locations of theoretical PMS evolutionary tracks and isochrones (e.g. Herczeg & Hillenbrand 2015). We use the online tool VO Sed Analyzer (VOSA)<sup>3</sup> to obtain the luminosity and temperature of the candidate PMS members in the clusters. This tool builds spectral energy distributions (SEDs) by using the  $J$ ,  $H$ ,  $K$  photometric data supplied along with the various online photometric catalogues in other wavelengths from 2MASS, FEPS, UKIDSS, *WISE*, VISTA, *Spitzer*, GLIMPSE, SDSS, Pan-STARRS, Dark Energy Survey, DECam and VPHAS<sup>4</sup> in the VO services, whenever available. We also input the distance and extinction information calculated in the previous sections for each cluster.

After correcting for the distance and extinction values, VOSA compares the observed SED with synthetic photometry obtained from theoretical models for solar metallicity (BT-Settl models, Allard 2014). Using the chi-squared minimization technique we obtain the best-fitting model and corresponding physical parameters such as luminosity, effective temperature, age, and mass for each source. SED fitting, however, does not work for the faint sources in our catalogue (e.g.  $J \sim 17$ – $18$  mag) as most of them do not have counterparts in other surveys. The H–R diagram of sources is depicted as a Hess diagram in Fig. 8. Evolutionary tracks and isochrones for various ages and masses from Baraffe et al. (2015) are shown as white dotted and continuous lines respectively. Since the SED-based membership analysis does not include a complete sample of members, the field-contaminated CMD-based membership analysis, which is more complete down to the low-mass end, was preferred for the IMF estimation. The SED analysis was used to obtain an average age of the member stars by fitting the PMS isochrones of Baraffe et al. (2015), as it gives more reliable age estimation compared to that from fitting isochrones directly on the NIR CMD.

Since most of our sample clusters are associated with gas and dust (e.g. Sharma et al. 2007; Koenig et al. 2008; Oliveira et al. 2009), their

<sup>3</sup><http://svo2.cab.inta-csic.es/theory/vosa/>

<sup>4</sup>Skrutskie et al. (2006), Carpenter et al. (2008), Lawrence et al. (2007), Wright et al. (2010), Evans et al. (2003), Churchwell et al. (2009), Ahn et al. (2012), Chambers et al. (2016), Dark Energy Survey Collaboration (2016), Drew et al. (2014).

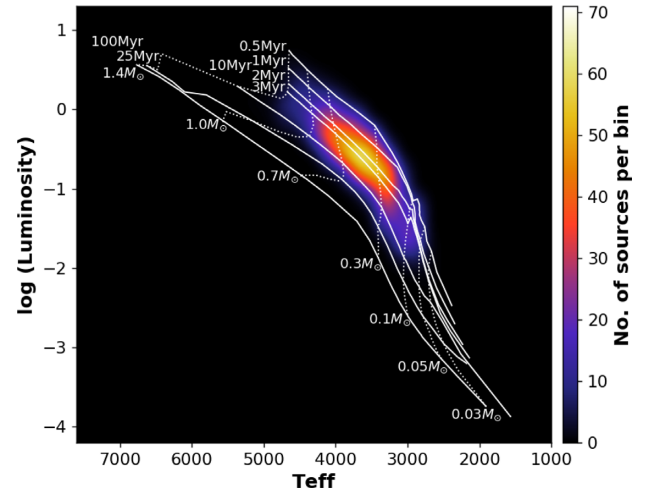


**Figure 8.** H–R diagram of all the sources in the sample cluster IC 1848–West with age  $< 10$  Myr. The luminosities and effective temperatures were obtained from the VOSA SED analysis. Evolutionary tracks and isochrones from Baraffe et al. (2015) are shown as white dotted and continuous lines respectively.

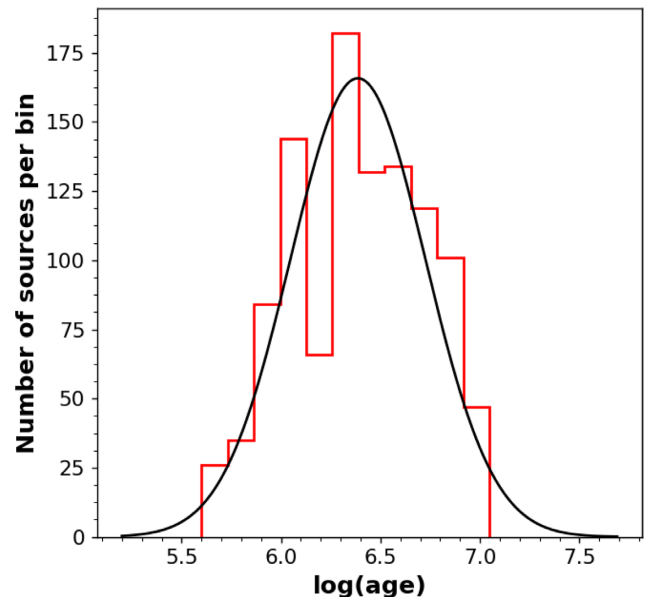


**Figure 9.** Histogram showing the age distribution of all the sources in the sample cluster IC 1848–West with age  $< 10$  Myr. The mean of the Gaussian fit gives the mean age of the cluster.

ages are likely to be less than 5 Myr (Leisawitz, Bash & Thaddeus 1989). We consider those sources with ages less than 10 Myr for estimating the mean age of the cluster by fitting a Gaussian curve. Fig. 9 shows the age distribution of the sample cluster IC 1848–West, fitted with the Gaussian curve. The mean age and age spread of the cluster is  $2.2 \pm 1$  Myr. We rounded the mean age derived from the Gaussian fit to the nearest whole number and the estimated mean age and age spread of each cluster are listed in Table 2. The mean age of our regions lies in the range  $\sim 1$ – $3$  Myr, implying that the clusters are indeed young and thus the effect of dynamical evolution is expected to be minimal.

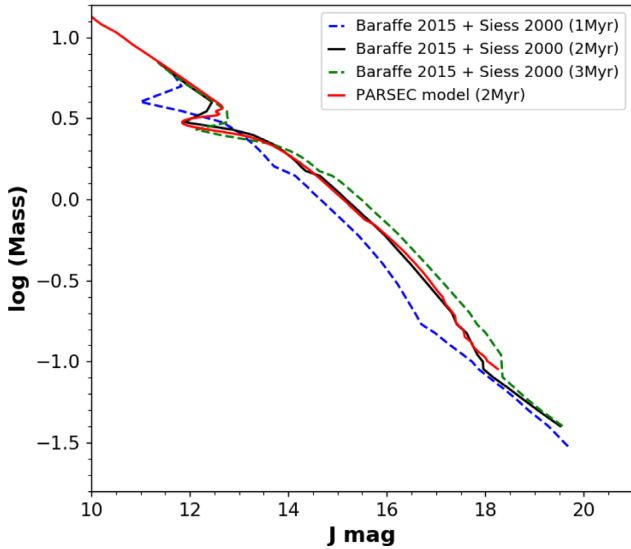


**Figure 10.** Mass–magnitude relation used for the IMF estimation of IC 1848-West. The black solid curve is for the 2 Myr isochrones from Baraffe et al. (2015) (for  $<1.4 M_{\odot}$ ) and Siess et al. (2000) (for  $>1.4 M_{\odot}$ ), respectively and the red curve is for the PARSEC model of 2 Myr (Bressan et al. 2012). The blue and green dashed curves are for 1 and 3 Myr from Baraffe et al. (2015) and Siess et al. (2000) isochrones, respectively.

### 3.7 Mass–magnitude relation

In order to estimate the mass of the individual members of the clusters, we incorporate the PMS stellar evolutionary models. For the mass–magnitude conversion, we use the Baraffe et al. (2015) models for sources with mass  $<1.4 M_{\odot}$  and the Siess, Dufour & Forestini (2000) models for mass  $>1.4 M_{\odot}$ , according to the respective cluster age. After correcting for the cluster distance and reddening, we convert the absolute magnitudes of the isochrones of respective ages for each cluster to apparent magnitudes. By fitting a polynomial to both models of the above mass range, we obtain a relation between mass and magnitude for the  $J$  and  $K$  bands. Using this relation, we estimate the mass of all the field-decontaminated candidate members within each cluster in the  $J$  and  $K$  bands (see Section 3.3). In Fig. 10 we present the mass–magnitude relation for the 2 Myr old cluster IC 1848-West in the  $J$  band. Our final IMF is estimated using the  $J$  and  $K$  bands independently in order to compare our results and check for any biases in the analysis.

The major sources of uncertainty in the above method to estimate the mass of PMS sources can be from the age spread and non-uniform reddening associated with the young clusters. However, for younger ages ( $<5$  Myr), the PMS isochrones in  $J$  versus  $J - H$  or  $J$  versus  $H - K$  planes are almost vertical (see Jose et al. 2017; Kuhn et al. 2017). This is because the colour change (in  $J - H$  or  $H - K$ ) of the low-mass PMS sources due to age variations within the range of  $\sim 2$ –5 Myr is negligible (see Siess et al. 2000; Pecaut & Mamajek 2013; Baraffe et al. 2015). Since the reddening variation within the clusters in our list is minimal (see Table 2), the above assumptions of mean age and mean reddening of the clusters are reasonably valid to estimate the mass–magnitude relation of the PMS sources. In order to check any uncertainty associated with possible age spread of the clusters in mass estimates (see Neichel et al. 2015), we overplot the isochrones of age 1 and 3 Myr from Siess et al. (2000) and Baraffe et al. (2015) in Fig. 10. The uncertainty in the mass–magnitude relation for  $\sim 2$  Myr age spread is of the order of the size of the mass bin

considered for IMF calculation (see Section 3.8) and hence we ignore this effect. Another form of uncertainty in the mass estimates of low-mass PMS members is from the lack of consistency among different stellar evolutionary models (e.g. Soderblom et al. 2014; Herczeg & Hillenbrand 2015 and references therein). In Fig. 10, we overplot the mass–magnitude curve for the PMS isochrone of 2 Myr age from PARSEC evolutionary models (Bressan et al. 2012). It is evident that the mass–magnitude relation of the PARSEC models matches that of the relation constructed from the 2 Myr isochrones from Siess et al. (2000) and Baraffe et al. (2015), and hence we ignore the effect of discrepancies among various PMS models in our analysis.

### 3.8 Initial mass function

In this section we discuss the distribution of IMFs in our study. Although observations of embedded clusters reveal the presence of binary systems within them that are difficult to resolve, as discussed in Section 1, the effect of binarity on IMF estimates is relatively small (Harayama et al. 2008; Mužić et al. 2017; Zeidler et al. 2017; Suárez et al. 2019) and hence we do not account for any unresolved companions in our analysis. The system IMF treats binaries and multiple systems as single stars rather than multiple stars and hence is ideal to compare with our observations. Thus the IMFs that we derive are the system IMFs (Lada & Lada 2003). We obtain the IMF for the field-decontaminated PMS sources (Section 3.3) and within 90 per cent photometric completeness (see Table 1), which are mostly in the magnitude range of  $\sim 13$ –18 mag (see Fig. 4 and online Appendix C) and mass range of  $\sim 3$ –0.08  $M_{\odot}$  (see Fig. 10). We calculate the system IMF by counting the number of stars in a logarithmic mass interval of bin size,  $\log(m) = 0.2$ .

Pioneering work done by Salpeter (1955) introduced a power law for the IMF of the form

$$\phi(\log m) = \frac{dN}{d \log m} \propto m^{-\Gamma} \quad (2)$$

where  $m$  is the mass of a star,  $N$  is the number of stars in a logarithmic mass range  $\log m + d \log m$ , and  $\Gamma$  was found to be  $\sim 1.35$ , which is generally referred as the Salpeter slope. Later it was recognized that the IMF was probably not a single power law over all stellar masses. Kroupa (2001) presented a multisegment power law, where the slope of the IMF at lower masses was found to be shallower than the Salpeter slope at higher masses. The logarithmic formalism of the IMF by Chabrier (2003) has also been widely used as it provides a description of the IMF as a lognormal function at the low-mass end and a power-law form above  $1 M_{\odot}$ .

In this analysis we describe the derived system IMF using the lognormal distribution, i.e.

$$\xi(\log m) \propto e^{-\frac{(\log m - \log m_c)^2}{2\sigma^2}} \quad (3)$$

where  $m_c$  is the characteristic mass (the mass at the peak of the distribution) and  $\sigma$  is the standard deviation.

Fig. 11 shows the individual IMFs of all the clusters obtained from the mass estimated from the  $J$  band (left) and from the  $K$  band (right). The error bars represent the associated Poisson errors and the continuous curves are the lognormal fits to the individual cluster IMFs. The respective characteristic mass  $m_c$  and  $\sigma$  (the spread in the lognormal distribution) are listed in Table 3 for each cluster. The peak mass of the individual cluster lies in the range of  $\sim 0.18$ –0.48  $M_{\odot}$  and  $\sigma$  is in the range of  $\sim 0.39$ –0.66.

We compare our results with a nearby young cluster IC 348, which is one of the well studied star-forming regions and has well characterized membership analysis by several studies. IC 348 resides

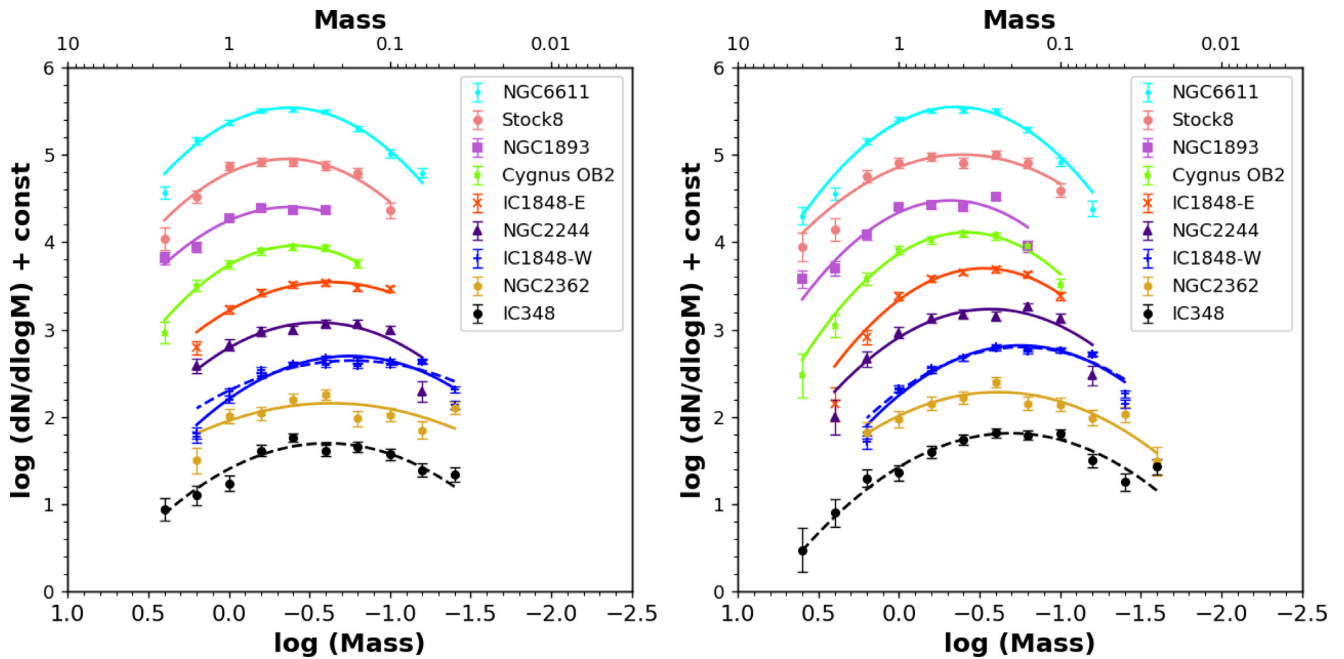


**Figure 11.** The IMF derived from the  $J$  band (left) and  $K$  band (right) for all the clusters. Error bars denote the Poisson error on each data point. The curves are the lognormal fits to the individual cluster IMF. The blue dotted curve shows the IMF estimated by applying the extinction correction to individual sources of the IC 1848-West cluster (see text).

**Table 3.** Characteristic mass ( $m_c$ ) and  $\sigma$  values from Fig. 11.

Cluster	<sup>a</sup> From fit		<sup>b</sup> From MC simulation			
	$J$ band	$K$ band	$J$ band		$K$ band	
	$m_c$ ( $M_\odot$ )	$\sigma$	$m_c$ ( $M_\odot$ )	$\sigma$	$m_c$ ( $M_\odot$ )	$\sigma$
IC 1848-West	$0.18 \pm 0.04$	$0.50 \pm 0.05$	$0.18 \pm 0.04$	$0.47 \pm 0.04$	$0.15 \pm 0.10$	$0.53 \pm 0.26$
IC 1848-East	$0.24 \pm 0.04$	$0.51 \pm 0.05$	$0.30 \pm 0.02$	$0.41 \pm 0.02$	$0.24 \pm 0.11$	$0.40 \pm 0.24$
NGC 1893	$0.42 \pm 0.05$	$0.45 \pm 0.06$	$0.48 \pm 0.06$	$0.40 \pm 0.07$	$0.38 \pm 0.15$	$0.37 \pm 0.22$
NGC 2244	$0.28 \pm 0.05$	$0.48 \pm 0.06$	$0.27 \pm 0.05$	$0.46 \pm 0.06$	$0.23 \pm 0.11$	$0.43 \pm 0.22$
NGC 2362	$0.23 \pm 0.13$	$0.66 \pm 0.18$	$0.24 \pm 0.06$	$0.55 \pm 0.07$	$0.13 \pm 0.05$	$0.46 \pm 0.26$
NGC 6611	$0.42 \pm 0.01$	$0.42 \pm 0.02$	$0.44 \pm 0.02$	$0.40 \pm 0.02$	$0.42 \pm 0.15$	$0.40 \pm 0.15$
Stock 8	$0.44 \pm 0.03$	$0.42 \pm 0.04$	$0.40 \pm 0.05$	$0.49 \pm 0.05$	$0.21 \pm 0.14$	$0.44 \pm 0.40$
Cygnus OB2	$0.39 \pm 0.01$	$0.41 \pm 0.02$	$0.38 \pm 0.02$	$0.39 \pm 0.02$	$0.31 \pm 0.14$	$0.40 \pm 0.18$
IC 348	$0.25 \pm 0.05$	$0.52 \pm 0.06$	$0.20 \pm 0.04$	$0.52 \pm 0.04$	– <sup>c</sup>	–
Mean	$0.32 \pm 0.02$	$0.49 \pm 0.02$	$0.32 \pm 0.01$	$0.45 \pm 0.02$	$0.26 \pm 0.04$	$0.43 \pm 0.08$
Mean <sup>d</sup>	$0.31 \pm 0.01$	$0.47 \pm 0.01$	$0.31 \pm 0.02$	$0.45 \pm 0.02$		

Notes. <sup>a</sup>Values obtained by fitting the individual IMF of the clusters, shown in Fig. 11.

<sup>b</sup>Values obtained by fitting the IMF after accounting for the various uncertainties through Monte Carlo simulations (see Section 3.9).

<sup>c</sup>For IC 348, a Monte Carlo simulation was not performed since the physical parameters were taken from Luhman et al. (2016).

<sup>d</sup>Values obtained after fitting the mean IMF of all the clusters, shown in Fig. 12.

in the Perseus molecular cloud and is one of the nearest ( $\sim 320$  pc; Ortiz-León et al. 2018) and richest star-forming regions with an age of  $\sim 2$ – $3$  Myr (Lada et al. 2006). Luhman et al. (2016) presents a complete census of members of IC 348 using optical and NIR spectral analysis. The data is nearly complete down to  $K < 16.8$  mag for  $A_J < 1.5$  mag, which corresponds to a mass limit of  $\sim 0.01 M_\odot$  for an age of  $\sim 3$  Myr. For comparison, we estimate the IMF of IC 348 by the same method as that of our clusters in this study. Using the source list from Luhman et al. (2016) and the mass–magnitude relation as mentioned in the previous section, we estimate the mass of the cluster members within IC 348. The IMF thus obtained for IC

348 is plotted along with our clusters in Fig. 11. The general form of the IMF and the values of  $m_c$  ( $0.25 M_\odot$ ) and  $\sigma$  ( $0.50$ ) of IC 348 are well consistent with the clusters in our list.

The mean values of  $m_c$  and  $\sigma$  for the IMF estimated from the  $J$  band are  $0.32 \pm 0.02 M_\odot$  and  $0.49 \pm 0.02$ ; those from the  $K$  band are  $0.32 \pm 0.01 M_\odot$  and  $0.45 \pm 0.02$ . In order to assess the effect of binning, the above analysis was repeated by shifting the mass bin by  $\log(m) = 0.1 M_\odot$  as well as by varying the bin sizes. After applying these variations, the difference in the estimated characteristic mass  $m_c$  and  $\sigma$  was found to agree within the uncertainty range for each cluster. As discussed in Sections 3.3 and 3.5 (also refer to online Appendix C)

the clusters exhibit minimal differential extinction within the area considered for the study, facilitating the use of an average extinction value in deriving the IMF. Nevertheless, to eliminate any uncertainties that might arise due to the consideration of uniform extinction in a cluster region, an extinction correction was applied to individual sources in the sample cluster IC 1848-West to obtain their absolute magnitudes. These absolute magnitudes were then compared to the PMS stellar evolutionary models to obtain their masses. With the newly obtained masses, the IMF of the IC 1848-West cluster was re-estimated as shown in Fig. 11 as a dashed curve. The values of  $m_c$  and  $\sigma$  estimated from the  $J$  band are  $0.17 \pm 0.07 M_\odot$  and  $0.61 \pm 0.09$  and from the  $K$  band are  $0.18 \pm 0.04 M_\odot$  and  $0.50 \pm 0.04$  respectively. The values of the characteristic mass ( $m_c$ ) and  $\sigma$  obtained by applying the extinction correction to individual sources are in agreement with the values estimated by applying average extinction to the cluster.

We also obtain the mean values of each mass bin in Fig. 11 after normalizing the peak value of IMF to one of the clusters, i.e. IC 1848-West, and obtain an empirical mean IMF of all the eight clusters in this study along with IC 348, which is shown in Fig. 12 (red curve). These mean values are tabulated in Table 4. The shaded region marks the 1 sigma deviation from the mean value in each mass bin. The IMF generally flattens out between 0.2 and 0.7  $M_\odot$  and then drops down on both sides, which is in agreement with the general form of the IMF of young clusters (Neichel et al. 2015; Maia et al. 2016; Moraux 2016; Jose et al. 2017; Suárez et al. 2019 and references therein). The lognormal fit to the above mean distribution (blue dashed curve) gives  $m_c = 0.31 \pm 0.01 M_\odot$  and  $\sigma = 0.47 \pm 0.01$  for the  $J$  band and  $m_c = 0.31 \pm 0.02 M_\odot$  and  $\sigma = 0.45 \pm 0.02$  for the  $K$  band. The mean IMF distribution of the clusters in this study correlates well with that of the Galactic field mass function, which has a characteristic mass  $m_c = 0.25 M_\odot$  and  $\sigma = 0.55$  (Chabrier 2003).

As discussed in Section 3.2, we have restricted our individual cluster radii to 3 sigma above the mean density of the background region in order to limit the differential reddening as well as field-star contaminants in a larger area. As a result, there are chances of exclusion for a few low-mass members lying beyond this radius for IMF estimates (e.g. due to primordial mass segregation, Andersen et al. 2017; Kaur et al. 2020). In order to test this, we estimate the IMF of a sample cluster, Stock 8, for a radius above the background density, i.e. 5 arcmin, which is  $\sim 2.3$  arcmin larger than the radius considered previously. We repeated the same process for this larger radius to obtain the IMF and the values for  $m_c$  and  $\sigma$  estimated using the  $J$  band are  $0.36 \pm 0.04 M_\odot$  and  $0.47 \pm 0.04$ , respectively. Within uncertainties, the  $m_c$  and  $\sigma$  values for larger radii are consistent with the values estimated for smaller radii. Therefore we consider that the effect of stars lying beyond the 3 sigma radius of the clusters on the overall shape of the IMF is unlikely to be significant.

Before we discuss the implications of our results, it is important to report some of the earlier IMF studies on these clusters. Jose et al. (2017) derived the IMF of Stock 8 using optical and deep IR data for a cluster radius of 3 arcmin. Their lognormal distribution to the low-mass end (0.08–1  $M_\odot$ ) yielded a peak mass of  $m_c = 0.43 M_\odot$ , which is consistent with our results. Mužić et al. (2019) studied the low-mass part of the IMF of NGC 2244 represented by two power laws. Although a direct comparison with our results is difficult, it is worth mentioning that Mužić et al. (2019) reported that there is no effect due to the lack/presence of massive OB stars on the formation efficiency of low-mass stars.

### 3.9 Monte Carlo simulations to assess various uncertainties

We have also assessed the impact of possible systematic bias on the IMF caused by the uncertainties associated with observational parameters such as distance, age, and extinction of the regions as well as the evolutionary models used. This assessment was done for all the clusters by employing Monte Carlo (MC) simulations using field-decontaminated sources by independently generating random values for the three parameters – age, distance, and extinction. For each of the three parameters we randomly generated 2000 values normally distributed within a range corresponding to their respective mean with dispersion equal to their errors listed in Table 2. Following this, 1000 iterations were processed wherein each iteration used a randomly picked set of values pertaining to the three parameters and the mass corresponding to the  $J$  band was estimated utilizing the same evolutionary models mentioned in Section 3.7 (i.e. Baraffe et al. 2015 models for sources with mass  $< 1.4 M_\odot$  and Siess et al. 2000 models for mass  $> 1.4 M_\odot$ ). Thus, using the mass obtained through each iteration, the respective IMF was constructed by fitting a lognormal function and  $m_c$  and  $\sigma$  were estimated. The average values of  $m_c$  and  $\sigma$  from the 1000 iterations for each cluster are tabulated in Table 3. The mean values of  $m_c$  and  $\sigma$  for the eight clusters are  $0.26 \pm 0.04$  and  $0.43 \pm 0.08$ , respectively. For the majority of the clusters, the values obtained from the simulations are within 3 sigma uncertainty of the values obtained from the fitting method above (see Section 3.8). Also, in order to account for any possible bias associated with the use of the Baraffe et al. (2015) models in the above IMF estimates of the clusters, we have done the MC simulations detailed above using a different model set (i.e. PARSEC evolutionary models; Bressan et al. 2012) for a sample cluster, IC 1848-West. The use of a different evolutionary model resulted in a marginal shift in the mean values of  $m_c$  and  $\sigma$  with  $m_c = 0.27 \pm 0.13 M_\odot$  and  $\sigma = 0.41 \pm 0.28$ , which are within the average values obtained for the eight clusters within 3 sigma listed in Table 3.

## 4 DISCUSSION

Embedded clusters are the basic units of star formation and their study can address some fundamental astrophysical problems like cluster formation and evolution through the form and universality of the stellar IMF. The embedded phase of cluster evolution appears to last between 2 and 5 Myr, and clusters with ages greater than 10 Myr are rarely associated with molecular gas (Leisawitz et al. 1989; Lada & Lada 2003). Several studies have been carried out to understand the nature of the IMF; the low-mass regime in particular has been the subject of numerous observational and theoretical studies over the past decade (see Offner et al. 2014 for a review).

### 4.1 Characteristic stellar mass and theoretical implications

The high-mass stars generally follow the Salpeter mass function (Salpeter 1955). However, the IMF is not so well constrained at lower masses and appears to flatten below 1  $M_\odot$  with a turnover between 0.1 and 0.7  $M_\odot$  (Chabrier 2003). The stellar mass at which this transition in the slope occurs is considered to depend generally on the physical properties of the underlying molecular cloud (Larson 2005; Elmegreen, Klessen & Wilson 2008). The peak of the IMF is a key constraint for star-formation models since it is not a scale-free parameter (unlike the high-mass slope) and thus additional physics beyond gravity-driven accretion or turbulence is required to set it (Krumholz 2014). Possibilities include the thermal Jeans mass (e.g. Larson 2005), the turbulent Jeans mass (e.g. Hennebelle & Chabrier 2008),

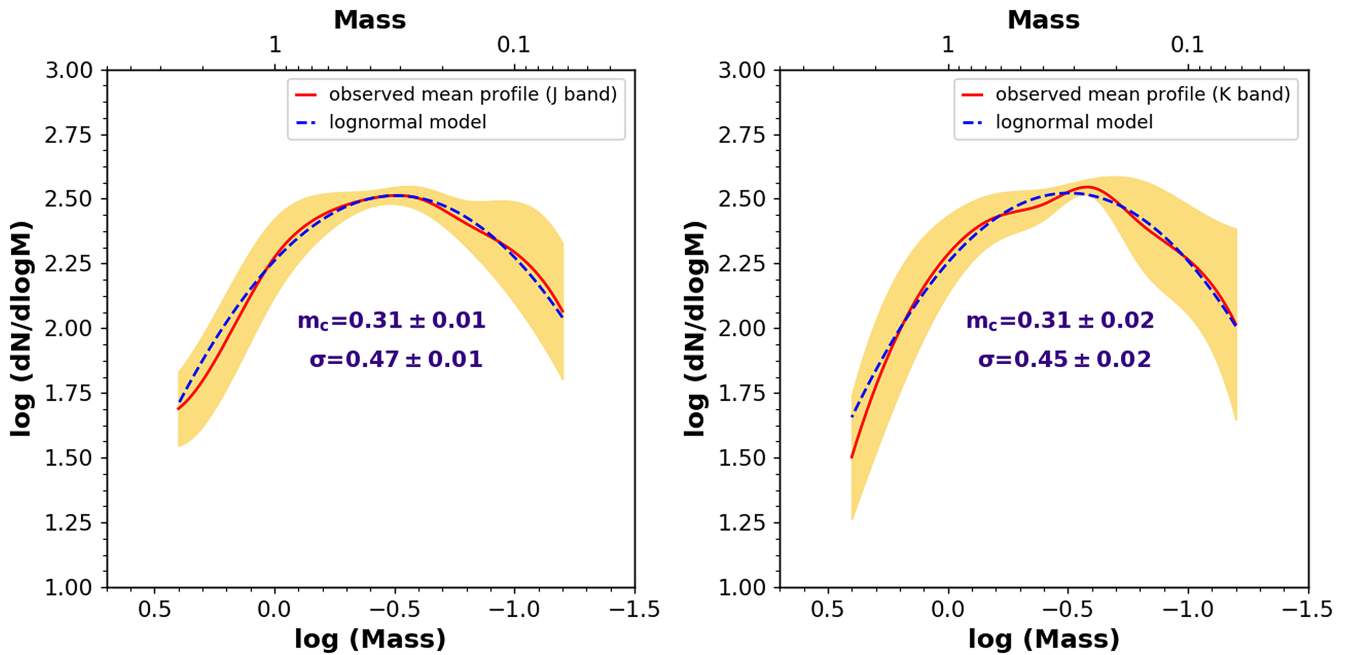


**Figure 12.** Mean IMF of all the eight clusters in the study including IC 348 (red curve) derived using the *J*-band magnitude (left) and the *K*-band magnitude (right). The blue dotted curve is the lognormal fit to the distribution. The shaded region marks the 1 sigma deviation from the mean.

**Table 4.** Mean  $\log(\text{Mass})$  and  $\log(dN/d \log M)$  values used for Fig. 12.

<i>J</i> band		<i>K</i> band	
$\log(\text{Mass})$	$\log(dN/d \log M)$	$\log(\text{Mass})$	$\log(dN/d \log M)$
-1.2	2.07	-1.2	2.02
-1.0	2.29	-1.0	2.27
-0.8	2.40	-0.8	2.41
-0.6	2.50	-0.6	2.54
-0.4	2.50	-0.4	2.48
-0.2	2.44	-0.2	2.43
0.0	2.27	0.0	2.28
0.2	1.95	0.2	1.99
0.4	1.69	0.4	1.50

radiative feedback (e.g. Bate 2009), and initial cloud density (e.g. Jones & Bate 2018). Predictions for how the IMF and in particular the peak mass of the IMF behaves in different environments change depending on which of these processes dominate. Simulation studies by Krumholz et al. (2016) suggest that radiative heating is the main driving mechanism of the characteristic mass of the IMF. This study shows that the efficiency of cloud fragmentation reduces as radiative heating increases, which eventually leads to a top-heavy IMF. On the other hand, Conroy & van Dokkum (2012) suggest that the radiative ambient pressure plays a significant role in generating bottom-heavy IMFs (at increasing pressure) as observed in elliptical galaxies with a history of starburst-generating mergers. Additional kinetic feedback such as stellar winds, protostellar outflows/jets, UV ionization etc. are also likely to affect the efficiency of star formation (e.g. Li & Nakamura 2006). However, it is still a matter of debate how and if they ultimately affect stellar-mass distribution, i.e. the IMF. Thus, exploring various star-forming environments is a valuable tool for understanding the standard form of the IMF (see Hosek et al. 2019).

In the standard picture of the star-formation process, beginning from the compression of gas in a GMC leading to the collapse and formation of protostars and their evolution into PMS objects

through accretion, different environmental conditions may play a role in shaping the final products like IMF (Prisinzano et al. 2011 and references therein). In this process, it has been shown that massive stars affect the evolution of their natal molecular clouds through their strong stellar winds and UV radiation (Murray, Quataert & Thompson 2010; Dale, Ercolano & Bonnell 2012; Walch et al. 2013; Rey-Raposo et al. 2017; Kim, Kim & Ostriker 2019). The ionizing UV radiation has strong competing effects on surrounding molecular cloud and subsequent star formation (e.g. Dale 2017; Gavagnin et al. 2017; Geen, Soler & Hennebelle 2017; Kim, Kim & Ostriker 2018; Kruijssen et al. 2019). One is negative feedback on the star-formation activity that disperses the remaining molecular cloud and truncates further star formation. The other is positive feedback as the interaction triggers new episodes of star formation (e.g. Deharveng et al. 2012; Jose et al. 2013; Samal et al. 2014; Jose et al. 2016; Panwar et al. 2019). Krumholz et al. (2016) suggest that radiation feedback is the key process in determining the location of the peak of the IMF. Considering that the clusters in this study are under diverse radiation environments (see below), it is therefore useful to understand the role of UV radiation feedback on the form of the IMF.

#### 4.2 IMF under diverse environmental conditions

We have carried out this study to test the universality of the IMF at the low-mass end down to the brown-dwarf limit for star-forming regions of diverse environmental conditions in terms of UV radiation, Galactic location, stellar density etc. We estimate the UV radiation field strength  $\log(L_{\text{FUV}}/L_{\odot})$  and  $\log(L_{\text{EUV}})$  from the respective massive stars present in each cluster listed in Section 2.1. UV luminosities corresponding to the spectral types are obtained from Guarcello et al. (2016) and Thompson (1984), and we add them for all the massive stars present in a given cluster. The eight clusters selected in this study are embedded in massive stellar environments of radiation field strength  $\log(L_{\text{FUV}}/L_{\odot}) \sim 5.07\text{--}6.81$  and  $\log(L_{\text{EUV}}) \sim 48.8\text{--}50.85$  photon  $\text{s}^{-1}$ , whereas, for IC 348, these values are  $\sim 2.6$

and  $\sim 42.2$  photon  $\text{s}^{-1}$ , respectively. These clusters are located at a heliocentric distance of  $\sim 1\text{--}4$  kpc ( $R_g \sim 6\text{--}12$  kpc) and the associated molecular cloud mass ranges from  $\sim 10^4\text{--}10^5 M_\odot$  (see references in Section 2.1). The peak stellar density at the cluster centres varies between  $\sim 170$  and  $1220$  stars  $\text{pc}^{-2}$ . The radiation strength, stellar density, cloud density, Galactocentric distance etc. vary by several orders among the clusters and hence these regions can be considered as in diverse environmental conditions. In Fig. 13 (top), we compare the characteristic mass distribution as a function of  $L_{\text{FUV}}$  for the nine clusters. We do not find any strong dependence of radiation field strength on the shape of the IMF (see Fig. 11) or on characteristic stellar mass (see Fig. 13) as a function of the above parameter.

In the disc of our Galaxy, a number of ISM properties are found to be varying as a function of Galactocentric distance (Rigby et al. 2019), such as metallicity (Caputo et al. 2001; Luck & Lambert 2011), molecular-to-atomic gas ratio (e.g. Sofue & Nakanishi 2016), interstellar radiation field (e.g. Popescu et al. 2017), and dust temperature (e.g. Urquhart et al. 2018). However, the outcome of various star-formation activities such as the clump-formation efficiency (or the dense-gas mass fraction), star-formation efficiency, or the physical properties of the molecular clumps do not seem to vary as a function of Galactocentric radius (see Moore et al. 2012; Eden et al. 2013, 2015; Rigby et al. 2019 and references therein). Similarly, one of the main outcomes of star-formation activity, the IMF, needs to be tested across various Galactocentric distances. In Fig. 13 (middle), we plot the characteristic stellar mass as a function of the Galactocentric radius and we do not find any systematic trend in  $m_c$  as a function of  $R_g$ . Also, the form of the low-mass end of the IMF does not vary with  $R_g$  (see Fig. 11). Similarly, in Fig. 13 (bottom) it is seen that the forms of the IMF or characteristic stellar mass do not show any systematic variation as a function of stellar density for the various clusters under this study. In summary, we do not observe any systematic variation in our analysis, implying no strong environmental effects on the clusters under this study.

### 4.3 Comparison with other regions

As discussed earlier, the behaviour of IMF in diverse environmental conditions is yet to be well understood. Some of the young star-forming regions in the solar neighbourhood whose IMFs down to the sub-solar regime have been extensively studied are discussed here. Among them, the Orion nebula cluster (ONC) located at  $\sim 470$  pc is reported to have a lognormal distribution at the low-mass end ( $\sim 0.02\text{--}3 M_\odot$ ) of the IMF with a characteristic mass of  $0.28 \pm 0.02 M_\odot$  and  $\sigma = 0.38 \pm 0.01$  (Da Rio et al. 2012). Similarly, an NIR survey of the nearby star-forming region,  $\sigma$  Orionis, by Peña Ramírez et al. (2012) shows that the low-mass end of the IMF has a similar distribution to that of other nearby young clusters, with a characteristic mass of  $0.27 \pm 0.07 M_\odot$  and  $\sigma = 0.57 \pm 0.11$  in the mass range  $0.006\text{--}19 M_\odot$ . Another such star-forming region is 25 Orionis (25 Ori) located at a distance of  $\sim 350$  pc and with an age of  $\sim 7\text{--}10$  Myr. Suárez et al. (2019) described the IMF of 25 Ori using various functional forms for different cluster radii. The lognormal fit to the derived IMF in the mass range of  $0.01\text{--}13 M_\odot$  for an area of  $0.5^\circ$  yields values of  $m_c$  and  $\sigma$  of  $0.31 \pm 0.06 M_\odot$  and  $0.51 \pm 0.08$ , respectively. Here we would like to note that, within uncertainties, the IMFs of all these nearby star-forming regions in the solar neighbourhood correlate well with our results for the eight young clusters, which are relatively distant and with diverse physical parameters and environmental conditions.

Likewise, we also compare our results with some of the most massive young Galactic star clusters like Westerlund 1, NGC 3603,

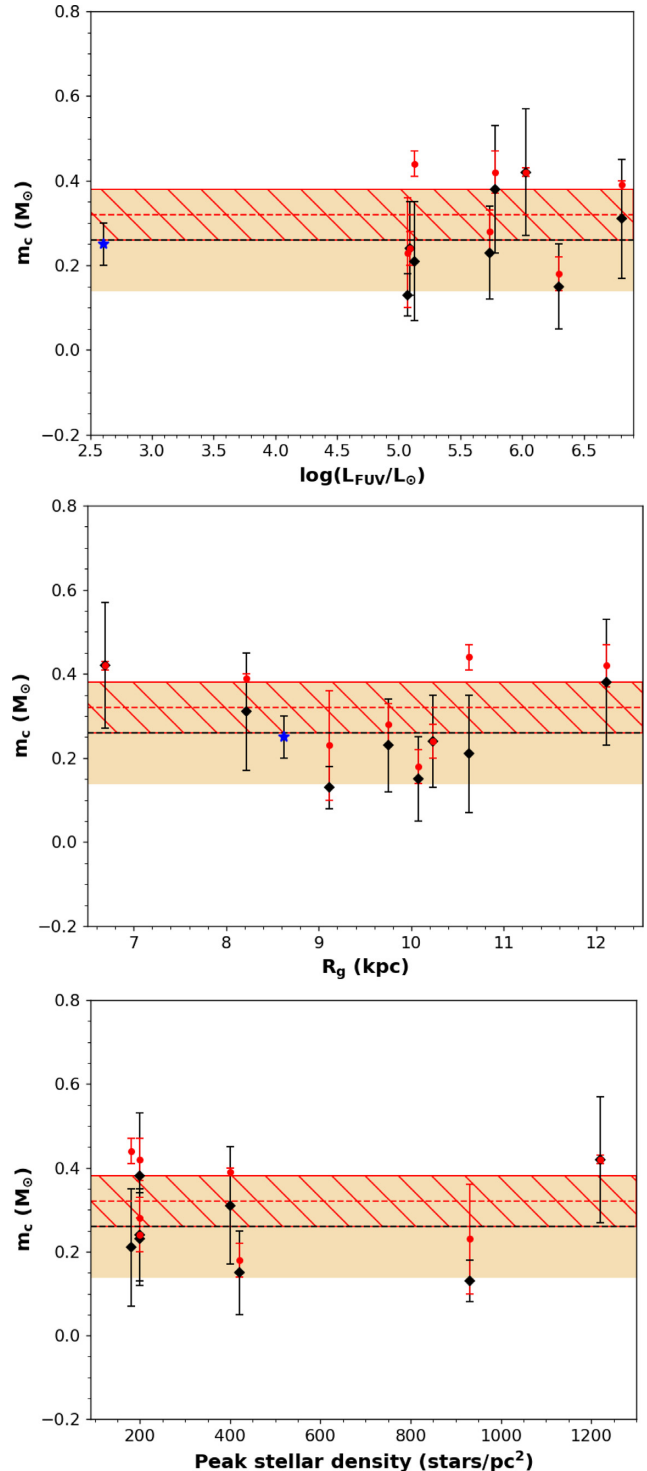


**Figure 13.** The distribution of characteristic stellar mass ( $m_c$ ) as a function of  $L_{\text{FUV}}$  (top), as a function of Galactocentric distance ( $R_g$ ) (middle), and as a function of peak stellar density (bottom) for the clusters obtained from Fig. 11 (red dots) and from Monte Carlo simulations (black dots). The blue source represents the nearby low-mass cluster IC 348. The red dashed line and hatched region represent the mean value of  $m_c = 0.32 M_\odot$  and 3 sigma deviation respectively from Fig. 11. The black dashed line and yellow shaded region mark the mean value of  $m_c = 0.26 M_\odot$  and 3 sigma deviation respectively, after accounting for the various sources of uncertainties using the Monte Carlo simulations.

and RCW 38. Westerlund 1 (Wd1) is a super massive cluster located at a distance of  $\sim 3.7\text{--}5$  kpc and of age  $\sim 3\text{--}5$  Myr. Using deep *HST* data, Andersen et al. (2017) derived the mass function of the supermassive cluster as a function of radius. They show that the flattening at the low-mass end of the IMF is similar to that of nearby low-mass star-forming regions and a lognormal fit to the IMF shows the width of the distribution of the sub-solar population to be comparable or slightly less than that of the Galactic field ( $\sigma \sim 0.33\text{--}0.44$ ). Another massive region is the luminous optically visible compact cluster NGC 3603 located at a distance of  $\sim 7$  kpc (Pandey, Ogura & Sekiguchi 2000) in the Carina arm of our Galaxy. The core of NGC 3603 contains a Trapezium-like system (HD 97950) with about 50 massive stars, which makes it analogous to the core of R136 in 30 Doradus in the Large Magellanic Cloud. Hence NGC 3603 is considered a local template of starburst regions in distant galaxies (Nürnberg & Petr-Gotzens 2002). A direct comparison of our results with the IMF of NGC 3603 is not feasible as most of the studies derive the power-law distribution of the IMF. Nevertheless, we report the observations of Sagar, Munari & de Boer (2001), which put forward the idea that the low-mass IMFs of NGC 3603 and other similar young clusters have no dependence on Galactic longitude,  $R_g$ , and cluster age. RCW 38 is another young ( $\sim 1$  Myr) massive dense star-forming region at a distance of  $\sim 1.7$  kpc (Wolk et al. 2006). Mužić et al. (2017) studied the low-mass end of the IMF using deep VLT data and concluded that there is no substantial evidence for the effect of high stellar densities and the presence of numerous massive stars on the formation efficiency of low-mass stars.

#### 4.4 Inference and interpretation of the universality of the IMF

We compare the results obtained in this study with similar studies across a broad range of star-forming regions. On one hand we compare the results with nearby star-forming regions in the solar neighbourhood whose low-mass and sub-stellar regimes of the IMF have been well constructed and on the other hand we compare them with Galactic young massive clusters like Westerlund 1. Overlapping the lognormal fit to the mass function of clusters in this study with a large number of open clusters and star-forming regions in the solar neighbourhood reveals that they are all consistent within the uncertainties over the same mass range (see Offner et al. 2014; Moraux 2016; Suárez et al. 2019). We find that our results are in agreement with the general form of IMF given in Bastian et al. (2010), stating that locally there does not appear to be any strong systematic variation in the IMF. That is, a lognormal distribution can well characterize the form of the IMF within  $0.08\text{--}3 M_\odot$  for the clusters in our list.

We conclude that there is no strong evidence for an effect that a combination of various stellar densities, location in the Galaxy, and/or OB stellar radiation might have on the underlying form of the IMF or characteristic mass among the clusters in this study and other resolved star-forming regions and the Galactic field. For all star-forming regions where star counts have been possible the stellar IMF appears to be very similar. The values of characteristic mass and  $\sigma$ , after assessing for the effect of various systematic uncertainties through Monte Carlo simulations, are found to be close to the measured average IMF of all clusters within 3 sigma. We note that, even if small variations between regions exist because of the environmental factors, they may be hidden in the noise introduced from various parameter estimations.

Some of the uncertainties present in this study are the limited completeness of the data towards the cluster centre due to crowding, not accounting for the multiplicity of various populations in each cluster, and the effect of mass segregation; due to these uncertainties

some of the probable low-mass cluster members in the outer region might have not been included in the IMF analyses. However, with the existing data sets, we are unable to resolve these issues. Future high-resolution imaging and spectroscopic analysis would help us resolve the above problems.

## 5 CONCLUSIONS

Beyond 500 pc from the Sun, in diverse environments at different Galactocentric radii where metallicity varies and massive stellar feedback may dominate, the IMF has been measured only incompletely and imprecisely. The main goal of this work is to understand the low-mass part of the IMF, and compare it with the well studied mass distributions in Galactic star-forming regions. Since young clusters ( $< 5$  Myr) are assumed to be less affected by dynamical evolution, their mass function can be considered as the IMF. We obtain the IMF of eight young clusters (age  $< 5$  Myr) located at  $\sim 1\text{--}4$  kpc distance ( $R_g \sim 6\text{--}12$  kpc) with a dense pre-main-sequence population and for the nearby cluster IC 348 down to the brown-dwarf regime. We use the deep near-IR data from the United Kingdom Infrared Deep Sky Survey (UKIDSS) and the Mayall Telescope at Kitt Peak National Observatory (KPNO) in the *J*, *H*, and *K* passbands along with *Gaia* DR2 data for the analysis. These clusters are embedded in massive stellar environments of radiation field strength  $\log(L_{\text{FUV}}/L_\odot) \sim 2.6\text{--}6.8$ ,  $\log(L_{\text{EUV}}) \sim 42.2\text{--}50.85$  photon  $\text{s}^{-1}$ , with stellar density in the range of  $\sim 170\text{--}1220$  star  $\text{pc}^{-2}$  and molecular cloud mass of  $\sim 10^4\text{--}10^5 M_\odot$ . After a careful structural analysis, field-star decontamination, and completeness correction, we obtain an unbiased uniformly sensitive sample of PMS members of the clusters down to the brown-dwarf regime and obtain their form of the IMF. The characteristic mass ( $m_c$ ) and  $\sigma$  values of these nine clusters lie in the range of  $\sim 0.18\text{--}0.48 M_\odot$  and  $\sim 0.39\text{--}0.66$  with a mean of  $0.32 \pm 0.02 M_\odot$  and  $0.47 \pm 0.02$ , respectively. After accounting for the various sources of uncertainties through Monte Carlo-based simulations, the mean values of  $m_c$  and  $\sigma$  are estimated to be within 3 sigma uncertainty of the above values. We compare the peak mass of the IMF as well as its low-mass end with the nearby low-mass star-forming regions and with various supermassive clusters across the Milky Way to test the role of environmental factors. We also check for any systematic variation with respect to the radiation field strength and stellar density as well as that of  $R_g$ . We conclude that there is no strong evidence for an effect that a combination of various stellar densities, location in the Galaxy, and/or OB stellar radiation might have on the underlying form of the IMF or characteristic mass among the clusters in this study. This work is the first of its kind to obtain the low-mass end of the IMF of a statistically rich sample of clusters using a unique method to verify the role of external factors in its universality.

## ACKNOWLEDGEMENTS

The authors are grateful to the referee for providing very constructive comments. This paper is based on data obtained as part of the UKIRT Infrared Deep Sky Survey. This publication made use of the data products from the Two Micron All Sky Survey (a joint project of the University of Massachusetts and the Infrared Processing and Analysis Center/California Institute of Technology, funded by NASA and NSF), archival data obtained with the *Spitzer Space Telescope* (operated by the Jet Propulsion Laboratory, California Institute of Technology, under a contract with NASA), the *Wide-field Infrared Survey Explorer* [a joint project of the University of California, Los Angeles, and the Jet Propulsion Laboratory (JPL), California Institute

of Technology (Caltech), funded by the National Aeronautics and Space Administration (NASA)], and the NOAO Science Archive, which is operated by the Association of Universities for Research in Astronomy (AURA), Inc., under a cooperative agreement with the National Science Foundation. This publication makes use of VOSA, developed under the Spanish Virtual Observatory project supported by the Spanish MINECO through grant AyA2017-84089. VOSA has been partially updated by using funding from the European Union's Horizon 2020 Research and Innovation Programme, under Grant Agreement No. 776403 (EXOPLANETS-A). BD and JJ acknowledge the DST-SERB, Government of India for the start-up research grant (No. SRG/2019/000664) for the financial support and SP acknowledges the DST-INSPIRE fellowship (No. IF180092) of the Department of Science & Technology, India for carrying out this work.

## DATA AVAILABILITY

The UKIDSS and MYStIX data sets were derived from the public-domain VizieR. The data sets for the W5 clusters will be available in a forthcoming paper. The data used to generate Fig. 11 will be shared on reasonable request to the corresponding author.

## REFERENCES

- Ahn C. P. et al., 2012, *ApJS*, 203, 21
- Allard F., 2014, in Booth M., Matthews B. C., Graham J. R., eds, Proc. IAU Symp. 299, Exploring the Formation and Evolution of Planetary Systems. Cambridge Univ. Press, Cambridge, p. 271
- Andersen M., Gennaro M., Brandner W., Stolte A., de Marchi G., Meyer M. R., Zinnecker H., 2017, *A&A*, 602, A22
- Baba D. et al., 2004, *ApJ*, 614, 818
- Bailer-Jones C. A. L., Rybizki J., Fousneau M., Mantelet G., Andrae R., 2018, *AJ*, 156, 58
- Baraffe I., Homeier D., Allard F., Chabrier G., 2015, *A&A*, 577, A42
- Bastian N., Covey K. R., Meyer M. R., 2010, *ARA&A*, 48, 339
- Bate M. R., 2009, *MNRAS*, 392, 1363
- Berlanas S. R., Wright N. J., Herrero A., Drew J. E., Lennon D. J., 2019, *MNRAS*, 484, 1838
- Bhardwaj A., Panwar N., Herczeg G. J., Chen W. P., Singh H. P., 2019, *A&A*, 627, A135
- Bica E., Bonatto C., Dutra C. M., 2003, *A&A*, 405, 991
- Bik A., Henning T., Wu S. W., Zhang M., Brandner W., Pasquali A., Stolte A., 2019, *A&A*, 624, A63
- Bonatto C., Bica E., 2009, *MNRAS*, 394, 2127
- Bonatto C., Santos J. F. C. J., Bica E., 2006, *A&A*, 445, 567
- Bressan A., Marigo P., Girardi L., Salasnich B., Dal Cero C., Rubele S., Nanni A., 2012, *MNRAS*, 427, 127
- Cappellari M. et al., 2012, *Nature*, 484, 485
- Caputo F., Marconi M., Musella I., Pont F., 2001, *A&A*, 372, 544
- Cardelli J. A., Clayton G. C., Mathis J. S., 1989, *ApJ*, 345, 245
- Carpenter J. M. et al., 2008, *ApJS*, 179, 423
- Casertano S., Hut P., 1985, *ApJ*, 298, 80
- Chabrier G., 2003, *PASP*, 115, 763
- Chambers K. C. et al., 2016, preprint ([arXiv:1612.05560](https://arxiv.org/abs/1612.05560))
- Chauhan N., Pandey A. K., Ogura K., Jose J., Ojha D. K., Samal M. R., Mito H., 2011, *MNRAS*, 415, 1202
- Chen L., de Grijs R., Zhao J. L., 2007, *AJ*, 134, 1368
- Churchwell E. et al., 2009, *PASP*, 121, 213
- Conroy C., van Dokkum P. G., 2012, *ApJ*, 760, 71
- Cutri R. M. et al., 2003, The IRSA 2MASS All-Sky Point Source Catalog, NASA/IPAC Infrared Science Archive. Available at: <http://irsa.ipac.caltech.edu/applications/Gator/>
- Dahm S. E., 2005, *AJ*, 130, 1805
- Dahm S. E., Hillenbrand L. A., 2007, *AJ*, 133, 2072
- Dale J. E., 2017, *MNRAS*, 467, 1067
- Dale J. E., Ercolano B., Bonnell I. A., 2012, *MNRAS*, 424, 377
- Da Rio N., Robberto M., Hillenbrand L. A., Henning T., Stassun K. G., 2012, *ApJ*, 748, 14
- Dark Energy Survey Collaboration, 2016, *MNRAS*, 460, 1270
- De Marchi G., Paresce F., Portegies Zwart S., 2005, in Corbelli E., Palla F., Zinnecker H., eds, The Initial Mass Function 50 Years Later, Vol. 327, Springer, Dordrecht, p. 77
- De Marchi G., Paresce F., Portegies Zwart S., 2010, *ApJ*, 718, 105
- Deharveng L. et al., 2012, *A&A*, 546, A74
- Delgado A. J., González-Martín O., Alfaro E. J., Yun J., 2006, *ApJ*, 646, 269
- Dib S., 2014, *MNRAS*, 444, 1957
- Drew J. E. et al., 2014, *MNRAS*, 440, 2036
- Dufton P. L. et al., 2006, *A&A*, 457, 265
- Dutta S., Mondal S., Joshi S., Jose J., Das R., Ghosh S., 2018, *MNRAS*, 476, 2813
- Eden D. J., Moore T. J. T., Morgan L. K., Thompson M. A., Urquhart J. S., 2013, *MNRAS*, 431, 1587
- Eden D. J., Moore T. J. T., Urquhart J. S., Elia D., Plume R., Rigby A. J., Thompson M. A., 2015, *MNRAS*, 452, 289
- Elmegreen B. G., Klessen R. S., Wilson C. D., 2008, *ApJ*, 681, 365
- Evans N. J. et al., 2003, *PASP*, 115, 965
- Evans C. J. et al., 2005, *A&A*, 437, 467
- Feigelson E. D. et al., 2013, *ApJS*, 209, 26
- Gaia Collaboration et al., 2016, *A&A*, 595, A1
- Gaia Collaboration et al., 2018, *A&A*, 616, A1
- Gavagnin E., Bleuler A., Rosdahl J., Teyssier R., 2017, *MNRAS*, 472, 4155
- Geen S., Soler J. D., Hennebelle P., 2017, *MNRAS*, 471, 4844
- Geha M. et al., 2013, *ApJ*, 771, 29
- Gennaro M. et al., 2018, *ApJ*, 855, 20
- Guarcello M. G., Prisinzano L., Micela G., Damiani F., Peres G., Sciortino S., 2007, *A&A*, 462, 245
- Guarcello M. G. et al., 2016, preprint ([arXiv:1605.01773](https://arxiv.org/abs/1605.01773))
- Guszejnov D., Hopkins P. F., Graus A. S., 2019, *MNRAS*, 485, 4852
- Hanson M. M., 2003, *ApJ*, 597, 957
- Harayama Y., Eisenhauer F., Martins F., 2008, *ApJ*, 675, 1319
- Hennebelle P., Chabrier G., 2008, *ApJ*, 684, 395
- Hensberge H., Pavlovski K., Verschuere W., 2000, *A&A*, 358, 553
- Herczeg G. J., Hillenbrand L. A., 2015, *ApJ*, 808, 23
- Herczeg G. J. et al., 2019, *ApJ*, 878, 111
- Hillenbrand L. A., Massey P., Strom S. E., Merrill K. M., 1993, *AJ*, 106, 1906
- Hillwig T. C., Gies D. R., Bagnuolo William G. J., Huang W., McSwain M. V., Wingert D. W., 2006, *ApJ*, 639, 1069
- Hosek M. W., Lu J. R., Anderson J., Najjarro F., Ghez A. M., Morris M. R., Clarkson W. I., Albers S. M., 2019, *ApJ*, 870, 44
- Jeffries R. D., 2012, in Reylé C., Charbonnel C., Schultheis M., eds, EAS Publ. Ser. Vol. 57, Low-Mass Stars and the Transition Stars/Brown Dwarfs - EES2011. EDP Sciences, Les Ulis, p. 45
- Jones M. O., Bate M. R., 2018, *MNRAS*, 478, 2650
- Jose J. et al., 2008, *MNRAS*, 384, 1675
- Jose J. et al., 2013, *MNRAS*, 432, 3445
- Jose J., Kim J. S., Herczeg G. J., Samal M. R., Biegging J. H., Meyer M. R., Sherry W. H., 2016, *ApJ*, 822, 49
- Jose J., Herczeg G. J., Samal M. R., Fang Q., Panwar N., 2017, *ApJ*, 836, 98
- Jose J. et al., 2020, *ApJ*, 892, 122
- Kaur H., Sharma S., Dewangan L. K., Ojha D. K., Durgapal A., Panwar N., 2020, *ApJ*, 896, 29
- Kim J.-G., Kim W.-T., Ostriker E. C., 2018, *ApJ*, 859, 68
- Kim J.-G., Kim W.-T., Ostriker E. C., 2019, *ApJ*, 883, 102
- King R. R., Naylor T., Broos P. S., Getman K. V., Feigelson E. D., 2013, *ApJS*, 209, 28
- Knödseder J., 2000, *A&A*, 360, 539
- Koenig X. P., Allen L. E., Gutermuth R. A., Hora J. L., Brunt C. M., Muzerolle J., 2008, *ApJ*, 688, 1142
- Kraus A. L., Herczeg G. J., Rizzuto A. C., Mann A. W., Slesnick C. L., Carpenter J. M., Hillenbrand L. A., Mamajek E. E., 2017, *ApJ*, 838, 150
- Kroupa P., 2001, *MNRAS*, 322, 231
- Kroupa P., Weidner C., Pflamm-Altenburg J., Thies I., Dabringhausen J., Marks M., Maschberger T., 2013, in Oswalt T. D., Gilmore G., eds,

- Planets, Stars and Stellar Systems, Vol. 5: Galactic Structure and Stellar Populations. Springer Science+Business Media, Dordrecht, p. 115
- Kruijssen J. M. D. et al., 2019, *Nature*, 569, 519
- Krumholz M. R., 2014, *Phys. Rep.*, 539, 49
- Krumholz M. R., Myers A. T., Klein R. I., McKee C. F., 2016, *MNRAS*, 460, 3272
- Kuhn M. A., Medina N., Getman K. V., Feigelson E. D., Gromadzki M., Borissova J., Kurtev R., 2017, *AJ*, 154, 87
- Kuhn M. A., Hillenbrand L. A., Sills A., Feigelson E. D., Getman K. V., 2019, *ApJ*, 870, 32
- Lada C. J., Lada E. A., 2003, *ARA&A*, 41, 57
- Lada C. J. et al., 2006, *AJ*, 131, 1574
- Larson R. B., 2005, *MNRAS*, 359, 211
- Lawrence A. et al., 2007, *MNRAS*, 379, 1599
- Leisawitz D., Bash F. N., Thaddeus P., 1989, *ApJS*, 70, 731
- Li J. Z., 2005, *ApJ*, 625, 242
- Li Z.-Y., Nakamura F., 2006, *ApJ*, 640, L187
- Lim B., Sung H., Kim J. S., Bessell M. S., Karimov R., 2014a, *MNRAS*, 438, 1451
- Lim B., Sung H., Kim J. S., Bessell M. S., Park B.-G., 2014b, *MNRAS*, 443, 454
- Lu J. R., Do T., Ghez A. M., Morris M. R., Yelda S., Matthews K., 2013, *ApJ*, 764, 155
- Lucas P. W. et al., 2008, *MNRAS*, 391, 136
- Luck R. E., Lambert D. L., 2011, *AJ*, 142, 136
- Luhman K. L., 2018, *AJ*, 156, 271
- Luhman K. L., Esplin T. L., Loutrel N. P., 2016, *ApJ*, 827, 52
- Maia F. F. S., Moraux E., Joncour I., 2016, *MNRAS*, 458, 3027
- Marco A., Negueruela I., 2016, *MNRAS*, 459, 880
- Marco A., Bernabeu G., Negueruela I., 2001, *AJ*, 121, 2075
- Marshall D. J., Robin A. C., Reylé C., Schultheis M., Picaud S., 2006, *A&A*, 453, 635
- Martins F., Mahy L., Hillier D. J., Rauw G., 2012, *A&A*, 538, A39
- Massey P., Johnson K. E., Degioia-Eastwood K., 1995, *ApJ*, 454, 151
- Moffat A. F. J., 1972, *A&AS*, 7, 355
- Moitinho A., Alves J., Huélmolo N., Lada C. J., 2001, *ApJ*, 563, L73
- Moore T. J. T., Urquhart J. S., Morgan L. K., Thompson M. A., 2012, *MNRAS*, 426, 701
- Moraux E., 2016, in EAS Publ. Ser. Vol. 80-81, Stellar Clusters: Benchmarks of Stellar Physics and Galactic Evolution - EES2015. EDP Sciences, Les Ulis, p. 73
- Murray N., Quataert E., Thompson T. A., 2010, *ApJ*, 709, 191
- Muzić K., Schödel R., Scholz A. e., Geers V. C., Jayawardhana R., Ascenso J., Cieza L. A., 2017, *MNRAS*, 471, 3699
- Muzić K., Scholz A., Peña Ramírez K., Jayawardhana R., Schödel R., Geers V. C., Cieza L. A., Bayo A., 2019, *ApJ*, 881, 79
- Nambiar S., Das S., Vig S., Gorthi R. S. S., 2019, *MNRAS*, 482, 3789
- Negueruela I., Marco A., Israel G. L., Bernabeu G., 2007, *A&A*, 471, 485
- Neichel B., Samal M. R., Plana H., Zavagno A., Bernard A., Fusco T., 2015, *A&A*, 576, A110
- Nürnberg D. E. A., Petr-Gotzens M. G., 2002, *A&A*, 382, 537
- Offner S. S. R., Clark P. C., Hennebelle P., Bastian N., Bate M. R., Hopkins P. F., Moraux E., Whitworth A. P., 2014, in Beuther H., Klessen R. S., Dullemond C. P., Henning T., eds, Protostars and Planets VI. Univ. Arizona Press, Tucson, AZ, p. 53
- Ojha D. K. et al., 2011, *ApJ*, 738, 156
- Oliveira J. M., Jeffries R. D., van Loon J. T., 2009, *MNRAS*, 392, 1034
- Ortiz-León G. N. et al., 2018, *ApJ*, 865, 73
- Pandey A. K., Ogura K., Sekiguchi K., 2000, *PASJ*, 52, 847
- Pandey A. K., Samal M. R., Chauhan N., Eswaraiiah C., Pandey J. C., Chen W. P., Ojha D. K., 2013, *New Astron.*, 19, 1
- Panwar N. et al., 2017, *MNRAS*, 468, 2684
- Panwar N., Pandey A. K., Samal M. R., Battinelli P., Ogura K., Ojha D. K., Chen W. P., Singh H. P., 2018, *AJ*, 155, 44
- Panwar N., Samal M. R., Pandey A. K., Singh H. P., Sharma S., 2019, *AJ*, 157, 112
- Park B.-G., Sung H., 2002, *AJ*, 123, 892
- Pecaut M. J., Mamajek E. E., 2013, *ApJS*, 208, 9
- Peña Ramírez K., Béjar V. J. S., Zapatero Osorio M. R., Petr-Gotzens M. G., Martín E. L., 2012, *ApJ*, 754, 30
- Pérez M. R., 1991, *Rev. Mex. Astron. Astrofis.*, 22, 99
- Pérez M. R., The P. S., Westerlund B. E., 1987, *PASP*, 99, 1050
- Popescu C. C., Yang R., Tuffs R. J., Natale G., Rushton M., Aharonian F., 2017, *MNRAS*, 470, 2539
- Prisinzano L., Sanz-Forcada J., Micela G., Caramazza M., Guarcello M. G., Sciortino S., Testi L., 2011, *A&A*, 527, A77
- Probst R. G. et al., 2004, in Moorwood A. F. M., Iye M., eds, SPIE Conf. Ser. Vol. 5492, Ground-based Instrumentation for Astronomy, SPIE, Bellingham, p. 1716
- Raucq F., Rauw G., Mahy L., Simón-Díaz S., 2018, *A&A*, 614, A60
- Reid M. J. et al., 2014, *ApJ*, 783, 130
- Rey-Raposo R., Dobbs C., Agertz O., Alig C., 2017, *MNRAS*, 464, 3536
- Rigby A. J. et al., 2019, *A&A*, 632, A58
- Rochau B. et al., 2011, *MNRAS*, 418, 949
- Sagar R., Munari U., de Boer K. S., 2001, *MNRAS*, 327, 23
- Salpeter E. E., 1955, *ApJ*, 121, 161
- Samal M. R. et al., 2014, *A&A*, 566, A122
- Samal M. R. et al., 2015, *A&A*, 581, A5
- Schmeja S., 2011, *Astron. Nachrichten*, 332, 172
- Sharma S., Pandey A. K., Ojha D. K., Chen W. P., Ghosh S. K., Bhatt B. C., Maheswar G., Sagar R., 2007, *MNRAS*, 380, 1141
- Siess L., Dufour E., Forestini M., 2000, *A&A*, 358, 593
- Skrutskie M. F. et al., 2006, *AJ*, 131, 1163
- Soderblom D. R., Hillenbrand L. A., Jeffries R. D., Mamajek E. E., Naylor T., 2014, in Beuther H., Klessen R. S., Dullemond C. P., Henning T., eds, Protostars and Planets VI. Univ. Arizona Press, Tucson, AZ, p. 219
- Sofue Y., Nakanishi H., 2016, *PASJ*, 68, 63
- Sota A., Maíz Apellániz J., Walborn N. R., Alfaro E. J., Barbá R. H., Morrell N. I., Gamén R. C., Arias J. I., 2011, *ApJS*, 193, 24
- Sota A., Maíz Apellániz J., Morrell N. I., Barbá R. H., Walborn N. R., Gamén R. C., Arias J. I., Alfaro E. J., 2014, *ApJS*, 211, 10
- Stolte A., Brandner W., Brandl B., Zinnecker H., 2006, *AJ*, 132, 253
- Suárez G., Downes J. J., Román-Zúñiga C., Cerviño M., Briceño C., Petr-Gotzens M. G., Vivas K., 2019, *MNRAS*, 486, 1718
- Swaters R. A., Valdes F., Dickinson M. E., 2009, in Bohlender D. A., Durand D., Dowler P., eds, ASP Conf. Ser. Vol. 411, Astronomical Data Analysis Software and Systems XVIII. Astron. Soc. Pac., San Francisco, p. 506
- Tapia M., Costero R., Echevarria J., Roth M., 1991, *MNRAS*, 253, 649
- Thompson R. I., 1984, *ApJ*, 283, 165
- Urquhart J. S. et al., 2018, *MNRAS*, 473, 1059
- Vallée J. P., 2008, *AJ*, 135, 1301
- van Dokkum P. G., Conroy C., 2010, *Nature*, 468, 940
- Walch S., Whitworth A. P., Bisbas T. G., Wünsch R., Hubber D. A., 2013, *MNRAS*, 435, 917
- Willis S., Marengo M., Allen L., Fazio G. G., Smith H. A., Carey S., 2013, *ApJ*, 778, 96
- Winter A. J., Clarke C. J., Rosotti G. P., 2019, *MNRAS*, 485, 1489
- Wolk S. J., Spitzbart B. D., Bourke T. L., Alves J., 2006, *AJ*, 132, 1100
- Wright E. L. et al., 2010, *AJ*, 140, 1868
- Wright N. J., Drew J. E., Mohr-Smith M., 2015, *MNRAS*, 449, 741
- Xue X. X. et al., 2008, *ApJ*, 684, 1143
- Zeidler P., Nota A., Grebel E. K., Sabbi E., Pasquali A., Tosi M., Christian C., 2017, *AJ*, 153, 122

## SUPPORTING INFORMATION

Supplementary data are available at [MNRAS](https://academic.oup.com/mnras/article/504/2/2557/6263736) online.

**Appendix A.** Field of view of the clusters

**Appendix C.** Cluster, control field and field decontaminated CMDs

Please note: Oxford University Press is not responsible for the content or functionality of any supporting materials supplied by the authors. Any queries (other than missing material) should be directed to the corresponding author for the article.

**APPENDIX B: COMPLETENESS HISTOGRAMS OF A FEW CONTROL FIELDS**

The completeness histograms of some of the control fields of the sample clusters in *J* and *K* bands are shown in Fig. B1.

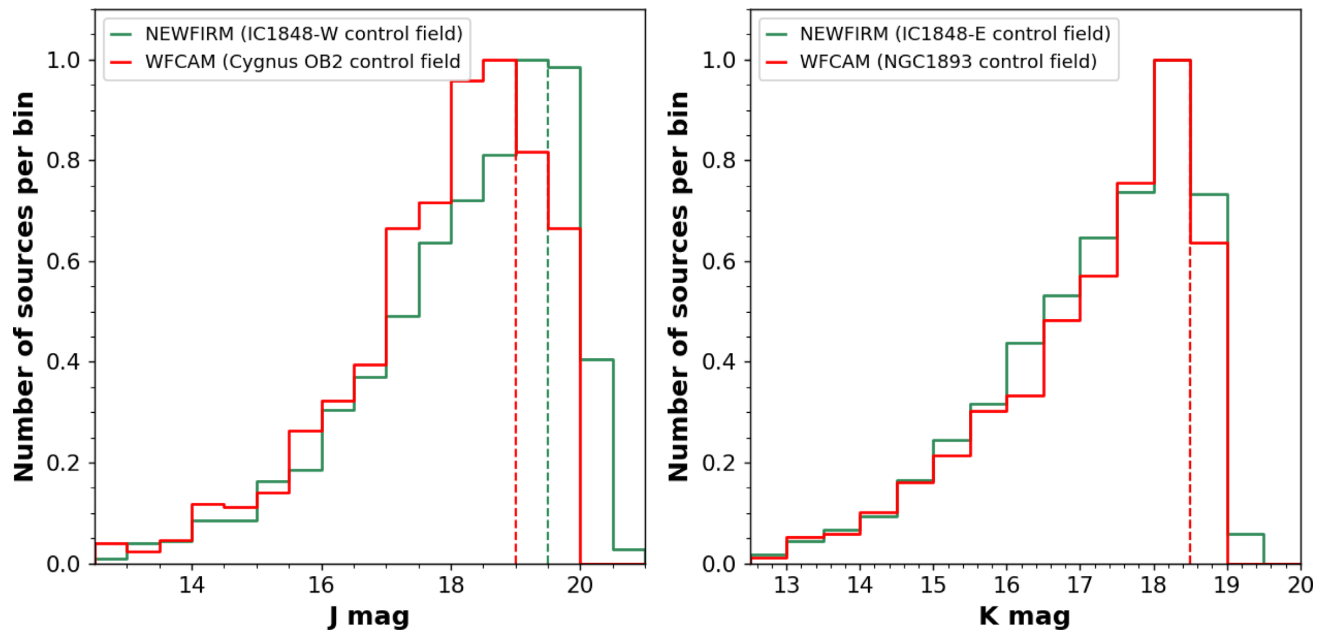


**Figure B1.** Normalized sample histograms showing the completeness limits of the control fields corresponding to the clusters in Fig. 2. The turnover point in the distribution serves as a proxy for the completeness limit of the data. The dashed lines mark the  $\sim 90$  per cent completeness limit of the photometry.

This paper has been typeset from a  $\text{\TeX}/\text{\LaTeX}$  file prepared by the author.